iScience

CellPress
OPEN ACCESS

Article

Electroacupuncture activates inhibitory neural circuits in the somatosensory cortex to relieve neuropathic pain

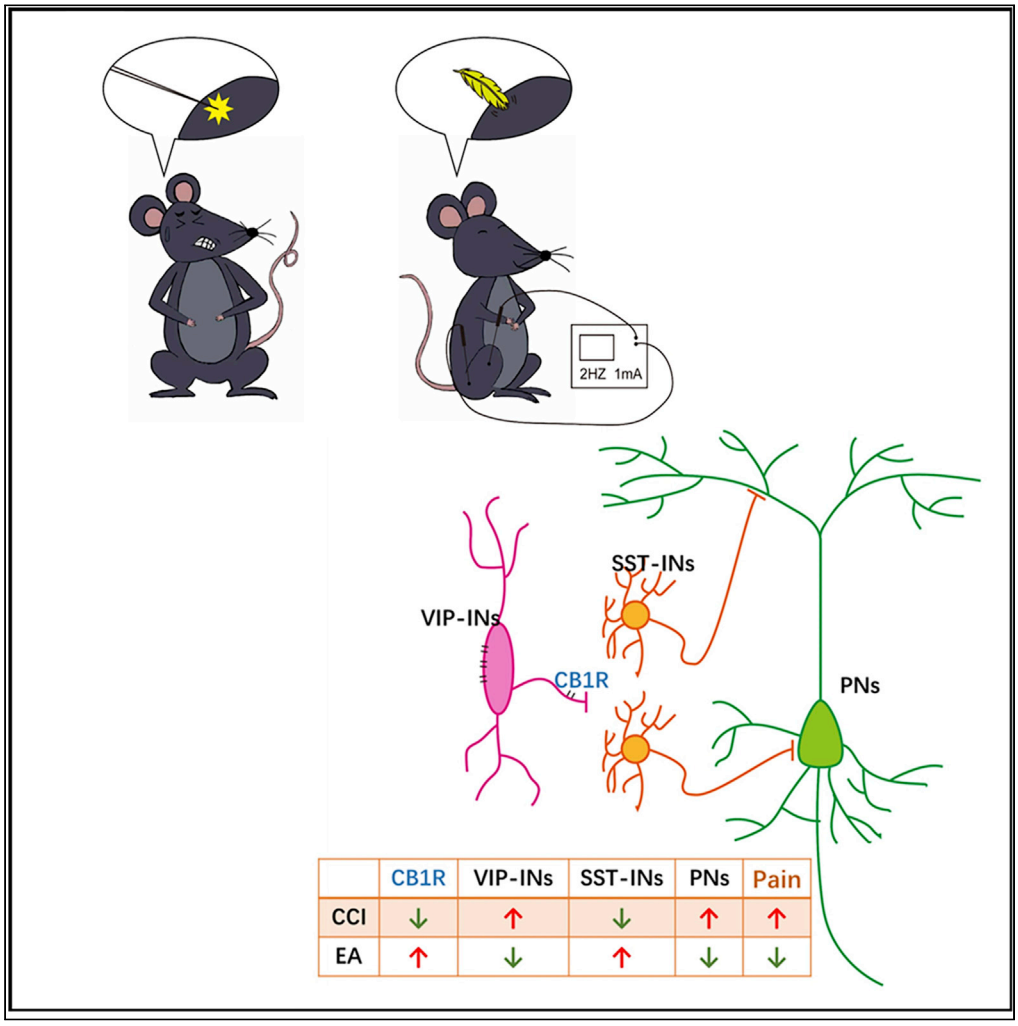

Ji-an Wei, Xuefei Hu, Borui Zhang, ..., Kwok-Fai So, Man Li, Li Zhang

liman73@mails.tjmu.edu.cn (M.L.)
zhangli@jnu.edu.cn (L.Z.)

HIGHLIGHTS

Electroacupuncture (EA) relieves mechanical hypersensitivity in neuropathic pain

EA restores normal excitatory-inhibitory transmission in sensory cortex

Endocannabinoid pathway underlies EA's effects via modulating inhibitory circuits

Wei et al., iScience *24*, 102066
February 19, 2021
https://doi.org/10.1016/j.isci.2021.102066

iScience

CellPress
OPEN ACCESS

Article

Electroacupuncture activates inhibitory neural circuits in the somatosensory cortex to relieve neuropathic pain

Ji-an Wei,[1,6] Xuefei Hu,[2,6] Borui Zhang,[1] Linglin Liu,[1] Kai Chen,[1] Kwok-Fai So,[1,3,4,5] Man Li,[2,*] and Li Zhang[1,4,5,7,*]

SUMMARY

Electroacupuncture (EA) has been accepted to effectively relieve neuropathic pain. Current knowledge of its neural modulation mainly covers the spinal cord and subcortical nuclei, with little evidence from the cortical regions. Using *in vivo* two-photon imaging in mice with chronic constriction injury, we found that EA treatment systemically modulated the Ca^{2+} activity of neural circuits in the primary somatosensory cortex, including the suppression of excitatory pyramidal neurons, potentiation of GABAergic somatostatin-positive interneurons, and suppression of vasoactive intestinal peptide-positive interneurons. Furthermore, EA-mediated alleviation of pain hypersensitivity and cortical modulation were dependent on the activation of endocannabinoid receptor 1. These findings collectively reveal a cortical circuit involved in relieving mechanical or thermal hypersensitivity under neuropathic pain and identify one molecular pathway directing analgesic effects of EA.

INTRODUCTION

Electroacupuncture (EA) effectively relieves various types of pain disorders as suggested by large amounts of clinical evidence (Ulett et al., 1998; Hinman et al., 2014; MacPherson et al., 2017; Scarborough and Smith, 2018; Hershman et al., 2018; Witt et al., 2005). To provide mechanistic explanations for the analgesic effects of acupuncture, classical views argue for the involvement of endorphins (Clement-Jones et al., 1980; Ho and Wen, 1989), and recent studies suggest the possible involvement of central opioids, monoamines, and neuropeptides (Zhang et al., 2014; Kim et al., 2009; Han, 2003). In particular, endocannabinoid receptor 1 (CB1R) pathway was recently found to be involved in central analgesic effects of EA (Yuan et al., 2018; Shou et al., 2013). All these neuromodulators may affect neural plasticity of the sensory pathway in the spinal cord (Xing et al., 2007; Koo et al., 2008) and brain (Zhao, 2008; Zhang et al., 2012) to reduce pain hypersensitivity. With regard to specific brain regions, EA-induced analgesia can be contributed by different subcortical nuclei, such as periaqueductal gray (PAG) (Guo et al., 2004), preoptic area (Ma et al., 2011), and habenular nucleus (Lee and Beitz, 1993). However, the somatosensory cortex has drawn little attention until a recent human brain imaging study suggested the rewiring of primary somatosensory cortex (S1) after continuous EA intervention (Maeda et al., 2017). Therefore, EA's analgesic functions may also involve the modulation of cortical circuits.

Pyramidal neurons (PNs) in S1 receive and send projections from and to various cortical and sub-cortical nuclei (Aronoff et al., 2010), making S1 a higher modulatory center for spatial and graded pain sensations (Bushnell et al., 1999). Recent findings further suggest the participation of S1-originated corticospinal tract (CST) in innervating dorsal horns of spinal cord to mediate pain sensitivity (Liu et al., 2018), illuminating a top-down modulatory pathway. Under neuropathic pain, both humans (Alshelh et al., 2016) and animal models (Liu et al., 2018; Cichon et al., 2017) have displayed the hyperactivity of S1 neurons, suggesting that the modulation of S1 activity might alleviate pain disorders.

Within S1, PNs are innervated by GABAergic interneurons (INs), forming a local circuit to code sensory inputs (Harris and Mrsic-Flogel, 2013; Huang and Paul, 2019). Two-photon *in vivo* imaging approach has illustrated the hyper-activation of layer 5 pyramidal neurons (L5PNs) and inhibition of INs of S1 in mice with neuropathic pain (Cichon et al., 2017). More importantly, the activation of somatostatin-positive INs (SST-INs) effectively reduced allodynia and hyperalgesia (Cichon et al., 2017). Such information provides

[1]Joint International Research Laboratory of CNS Regeneration, Guangdong-Hong Kong-Macau Institute of CNS Regeneration, Jinan University, Guangzhou, P. R. China

[2]Department of Neurobiology, School of Basic Medicine, Tongji Medical College, Huazhong University of Science and Technology, Wuhan, P. R. China

[3]State Key Laboratory of Brain and Cognitive Science, Li Ka Shing Faculty of Medicine, The University of Hong Kong, Hong Kong SAR, P. R. China

[4]Center for Brain Science and Brain-Inspired Intelligence, Guangdong-Hong Kong-Macao Greater Bay Area, Guangzhou 510515, P. R. China

[5]Guangzhou Regenerative Medicine and Health Guangdong Laboratory, Guangzhou 510530, P. R. China

[6]These authors contributed equally

[7]Lead contact

*Correspondence: liman73@mails.tjmu.edu.cn (M.L.), zhangli@jnu.edu.cn (L.Z.)

https://doi.org/10.1016/j.isci.2021.102066

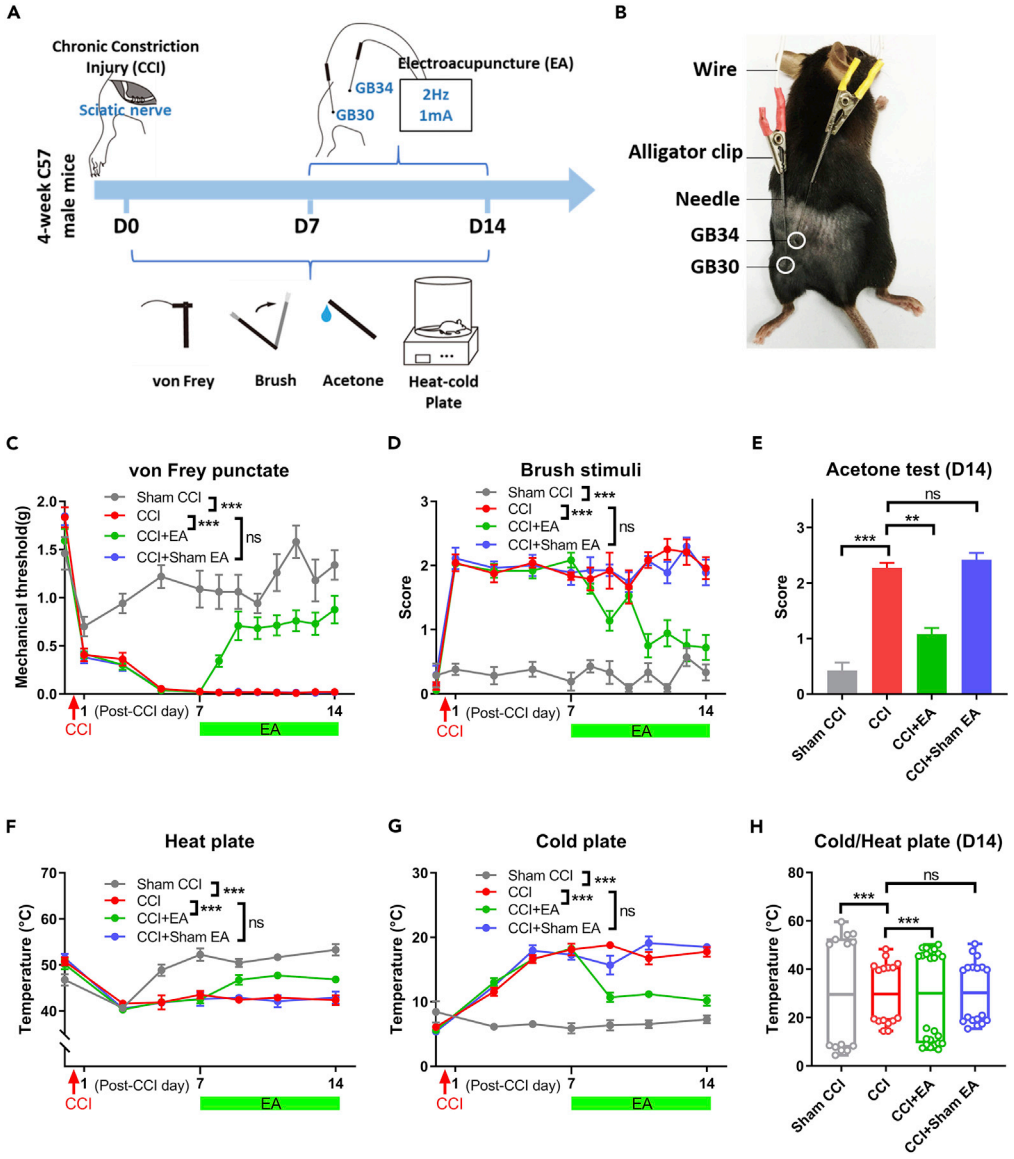

Figure 1. Electroacupuncture effectively relieves mechanical and thermal hypersensitivity

(A) Experimental outlines for (C–G). Male C57BL/6 mice received chronic constriction injury (CCI) surgery on D0 and received daily electroacupuncture (EA) for 7 days starting from D7. Both mechanical (von Frey and brush) and thermo-related (acetone and heat-cold plate) pain behaviors were continuously monitored for 14 days.

(B) A representative picture for EA treatment on mice. Two acupoints, GB30 (Huantiao) and GB34 (Yanglingquan), were adopted using standard acupuncture needles connected with electrical currents (1 mA, 2 Hz).

(C) Mechanical threshold of hindlimb retraction reflex using von Frey apparatus from D1 to D14 (two-way ANOVA, group f actor: $F(3, 32) = 125.7$, $p < 0.001$; time factor, $F(11, 352) = 61.72$, $p < 0.001$; ***$p < 0.001$ using Bonferroni post-hoc comparison; ns, no significant difference; $n = 7$, 8, 12, and 9 animals for sham CCI, CCI, CCI + EA, and CCI + sham EA group, respectively).

(D) Total scores for the brush-induced reflex, with higher score indicating stronger response (two-way ANOVA, group factor: $F(3, 32) = 162.4$, $p < 0.001$; time factor, $F(11, 352) = 23.60$, $p < 0.001$; ***$p < 0.001$ using Bonferroni post-hoc comparison; ns, no significant difference; $n = 7$, 8, 12, and 9 animals for sham CCI, CCI, CCI + EA, and CCI + sham EA group, respectively).

(E) Scores for acetone-induced reflex on D14, with higher score indicating stronger response (1-way ANOVA: $F(3, 31) = 62.91$, $p < 0.001$; ***$p < 0.001$ between sham CCI and CCI group; **$p = 0.0024$ between CCI and CCI + EA group; ns, no significant difference between CCI and CCI + sham EA group; Tukey's post-hoc comparison was used; $n = 8$, 8, 10, and 9 animals for sham CCI, CCI, CCI + EA, and CCI + sham EA group, respectively).

Figure 1. *Continued*

(F) Lowest temperature (heat threshold) of limb retraction on the heat plate (two-way ANOVA, group factor: $F(3, 32) = 41.26$, $p < 0.001$; time factor, $F(6, 192) = 31.53$, $p < 0.001$; ***$p < 0.001$ using Bonferroni post-hoc comparison; ns, no significant difference; $n = 7$, 8, 12, and 9 animals for sham CCI, CCI, CCI + EA, and CCI + sham EA group, respectively).

(G) Threshold of mice on the cold plate test (two-way ANOVA, group factor: $F(3, 32) = 118.0$, $p < 0.001$; time factor, $F(6, 192) = 62.25$, $p < 0.001$; ***$p < 0.001$ using Bonferroni post-hoc comparison; ns, no significant difference; $n = 7$, 8, 12, and 9 animals for sham CCI, CCI, CCI + EA, and CCI + sham EA group, respectively).

(H) Both heat and cold thresholds of mice on D14 were plotted to give the temperature sensation range (=heat threshold – cold threshold; one-way ANOVA: $F(3, 32) = 73.40$, $p < 0.001$; ***$p < 0.001$ using Tukey post-hoc comparison; ns, no significant difference; $n = 7$, 8, 12, and 9 animals for sham CCI, CCI, CCI + EA, and CCI + sham EA group, respectively). Data are presented as mean ± SEM.

a panoramic view of cortical neural circuits for pain sensation, and since the activation of cortical GABAergic transmission is sufficient to alleviate chronic pain behaviors (Eto et al., 2012), we thus propose that EA might modulate the excitatory-inhibitory (E/I) balance of S1 local circuits to alleviate neuropathic pain.

To test this hypothesis, we performed two-photon imaging of neuronal Ca^{2+} activities on both PNs and INs of S1, in a mouse neuropathic pain model receiving persistent EA treatment. In addition to reducing mechanical or thermal hypersensitivity in pain model animals, EA effectively suppressed the hyperactivity of L5PNs, and potentiated cortical GABAergic networks. Furthermore, we found that the CB1R activation was necessary for EA-mediated analgesic effects. These results collectively reported a cortical mechanism of EA in alleviating neuropathic pain.

RESULTS

EA relieves mechanical and thermal hypersensitivity under neuropathic pain

To substantiate analgesic effects of EA on patients with neuropathic pain, we adopted a mouse chronic constriction injury (CCI) model. One week after CCI surgery, mice were subjected to 7-day EA treatment (one session per day). During each EA treatment session, two acupoints, GB30 (Huantiao) and GB34 (Yanglingquan), were inserted with needles connecting to a pulsed current (amplitude: 1 mA; duration: 0.1 ms; frequency: 2 Hz; total length: 30 min; Figures 1A and 1B; see Transparent methods for more details). We found that either CCI surgery or EA treatment did not significantly change the animals' general locomotor activity or anxiety levels (Figure S1). When examining the mechanical pain threshold, CCI mice rapidly and persistently presented hypersensitivity under von Frey or brush stimuli test. In contrast, mice with EA treatment showed a marked elevation of mechanical pain thresholds (Figures 1C and 1D). The sham EA treatment (by inserting two needles into the adjacent regions of acupoints without applying the current) did not result in significant improvements of mechanical hypersensitivity (Figures 1C and 1D), suggesting specificity of EA-induced pain-relieving effects.

Given the existence of thermal hypersensitivity with neuropathic pain (Jensen and Finnerup, 2014), we investigated if EA also relieves such thermal stimuli-associated pain behaviors. Using the acetone dropping test, we found that EA, but not sham treatment, reduced the excessive occurrence of hindlimb retraction reflex in CCI mice (Figure 1E). Moreover, during a conventional heat/cold plate test, CCI model mice exhibited hypersensitivity by presenting lower thresholds upon heat stimuli, and higher thresholds when facing cold challenges, and EA treatment restored the normal cold-heat sensory range (Figures 1F–1H). These data collectively suggest that EA relieves both mechanical and heat/cold hypersensitivity under neuropathic pain.

EA treatment reduces pyramidal neuron hyperactivity in S1

To investigate the changes of neural circuits underlying the effects of EA in relieving pain hypersensitivity, we studied the activity of S1, which is potentiated across different neuropathic pain models (Cichon et al., 2017; Liu et al., 2018). Examining the expression of immediate early genes (IEGs), c-Fos, we found a significant increase in the number of activated neurons in S1 at 14 days after CCI surgery (D14), whereas EA treatment prevented such neuronal activation by CCI, especially at layer 5 (Figures S2A–S2C and Table S1). Double immunostaining further showed that a large number of excitatory neurons (Neurogranin+) in S1 were activated by CCI treatment and were inhibited after EA intervention (Figure S2D and Table S1). Therefore, EA potentially relieves the hyperactivity of excitatory neurons in S1 in neuropathic pain.

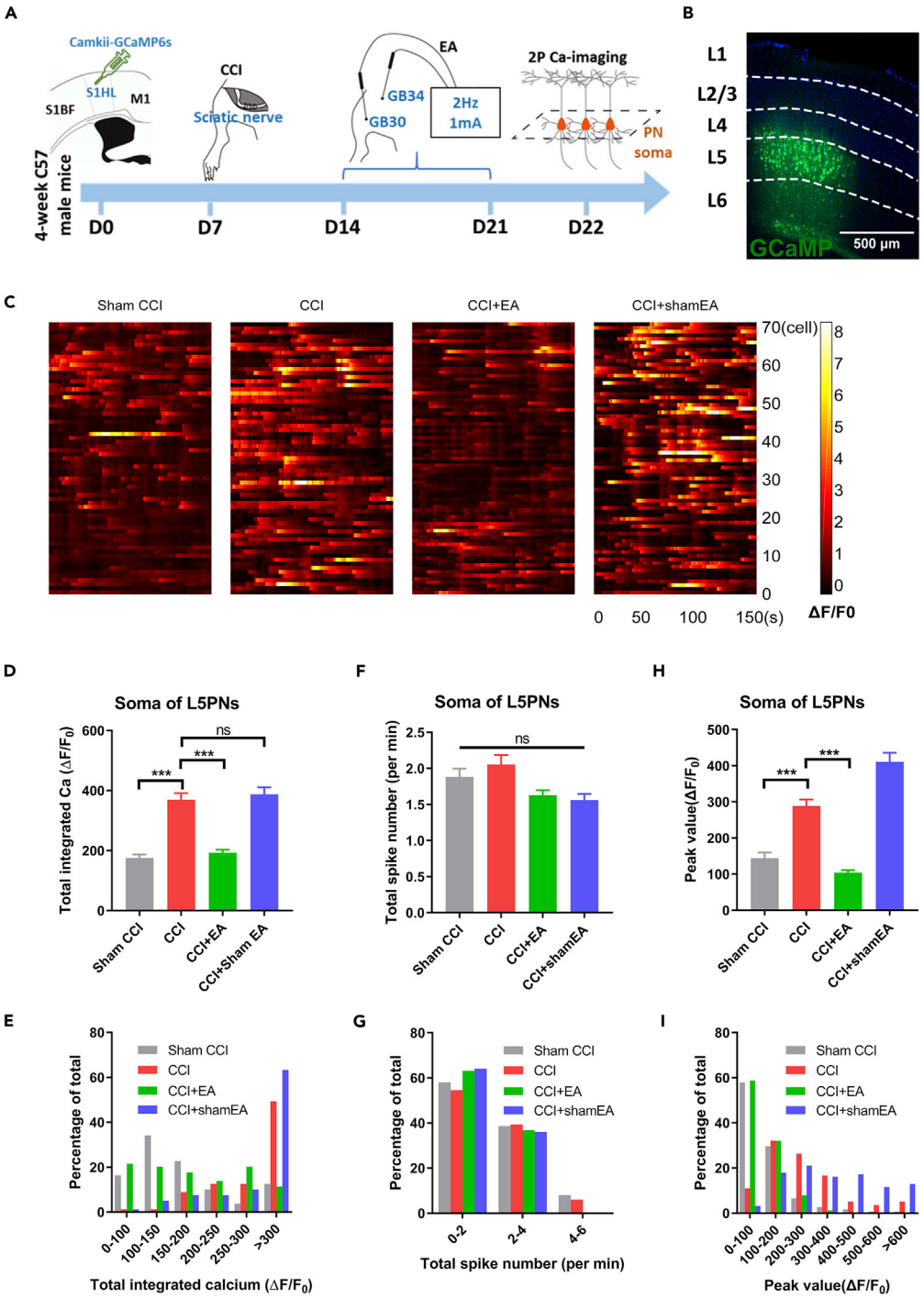

Figure 2. EA prevented hyperactivity of L5PNs *in vivo*

(A) Schematic diagrams for experiments in (C to I). Male C57BL/6 mice received transfection of AAV-Camkii-GCaMP6s into the S1 hindlimb (S1HL) region on one side, and were prepared for CCI surgery on the contralateral side on D7. EA treatment was performed from D14, and two-photon imaging was performed at 24 h after the conclusion of EA (D22).

(B) Transfection sites showing GCaMP6s expression mainly in layer 5. Scale bar, 500 μm.

(C) Time-elapse heat maps showing Ca^{2+} activities of L5PNs during a 150-s recording window. All data have been normalized to resting levels ($\Delta F/F_0$). A total of 70 representative neurons were plotted in each group.

(D and E) Total integrated Ca^{2+} activities of L5PNs. (D) Bar chart showing averaged total integrated Ca^{2+} activities (sham CCI: 175.8 ± 11.13, CCI: 369.9 ± 21.45, CCI + EA: 193.3 ± 10.17, CCI + Sham EA: 388.0 ± 23.00; Kruskal-Wallis test

Figure 2. *Continued*

statistic = 115.6, $p < 0.001$; ***$p < 0.001$ using Dunn's post-hoc comparison; ns, no significant difference; $n = 79, 67, 82,$ and 74 neurons, $N = 4, 5, 5,$ and 4 animals for sham CCI, CCI, CCI + EA, and CCI + sham EA group, respectively). (E) Histogram showing frequency distribution of total integrated Ca^{2+} activities.

(F and G), Total Ca^{2+} spike number (per min) of L5PNs. (F) Averaged Ca^{2+} spike frequency (sham CCI: 1.88 ± 0.11, CCI: 2.06 ± 0.13, CCI + EA: 1.63 ± 0.07, CCI + sham EA: 1.56 ± 0.09; ns, no significant difference from Kruskal-Wallis test; $n =$ 62, 66, 56, and 74 neurons, $N = 4, 5, 5,$ and 4 animals for sham CCI, CCI, CCI + EA, and CCI + sham EA group, respectively). (G) Histogram for the frequency distribution of Ca^{2+} spike frequency.

(H and I) Peak values of Ca^{2+} activities in L5PNs.

(H) Averaged peak values of Ca^{2+} activities (sham CCI: 144.4 ± 15.30, CCI: 288.7 ± 17.69, CCI + EA: 104.2 ± 6.92, CCI + sham EA: 410.6 ± 25.62; Kruskal-Wallis test statistic = 141.8, $p < 0.001$; ***$p < 0.001$ using Dunn's post-hoc comparison; $n = 68, 73, 61,$ and 80 neurons, $N = 4, 5, 5,$ and 4 animals for sham CCI, CCI, CCI + EA, and CCI + sham EA group, respectively).

(I) Frequency distribution of peak values of Ca^{2+} activities. Data are presented as mean ± SEM.

To provide *in vivo* evidence for the neuronal activity of S1, we employed two-photon Ca^{2+} imaging on L5PNs at the end of 7-day EA treatment (Figure 2A). By transfecting the fluorescent Ca^{2+} indictor GCaMP6s into L5PNs using an adeno-associated virus vector (Figure 2B), we recorded Ca^{2+} activities of pyramidal neuron somas in awake, head-fixed animals. From the continuous recording of 65∼80 live neurons per group (from 4∼5 animals per group), CCI animals had significantly higher Ca^{2+} activities compared with sham control group, whereas EA treatment remarkably alleviated Ca^{2+} hyperactivation of L5PNs (Figure 2C). Further data analysis showed that both total integrated Ca^{2+} activities (Figures 2D and 2E) and peak values of single Ca^{2+} spike (Figures 2H and 2I) were significantly elevated in CCI group, and were suppressed after EA but not sham EA treatment. On the other hand, the frequency of Ca^{2+} spikes (defined as the total spike number per minute) was not significantly changed across groups (Figures 2F and 2G).

L5PNs vertically extend their apical dendrites to form highly branched networks in the cortical superficial layer, where large amounts of dendritic spines reside to receive presynaptic inputs from both cortical and sub-cortical nuclei (Manns et al., 2004). We next examined the Ca^{2+} activity of dendritic spines in apical tuft (Figure 3A). Similar to the findings of L5PNs, CCI treatment potentiated Ca^{2+} spikes in apical spines, whose activities were significantly suppressed by EA intervention (Figure 3B). Further analysis showed that total integrated Ca^{2+} values (Figures 3C and 3D), Ca^{2+} spike frequency (Figures 3E and 3F), and peak values (Figures 3G and 3H) were all elevated in CCI model, and EA intervention mainly suppressed the frequency but not peak values, suggesting possible presynaptic inhibition. Combining *in vivo* recording data from both soma and dendritic spines of L5PNs, EA treatment relieved the hyperactivity of Ca^{2+} spikes induced by CCI. As L5PNs are the major inter- and sub-cortical projecting cells in S1 (Manns et al., 2004), EA-induced modulation on L5PNs may further affect the activity of other brain regions in the pain pathway.

In addition to L5PNs, we also recorded the activity of PN in layer 2/3 (L2/3 PNs) of S1. Both peak values and frequencies of Ca^{2+} spikes were increased by CCI treatment and were suppressed after EA intervention (Figure S3). In summary, EA treatment relieves the hyperactivity of PNs in S1 of mice with neuropathic pain.

EA normalized cortical inhibitory network

Cortical PNs are under a tight control of various subtypes of INs. As we found significantly elevated c-Fos activity of S1 GABAergic neurons in EA-treated mice (Figure S4 and Table S1), it should be valuable to monitor *in vivo* activities of INs. As SST-INs intensively innerve L5PN apical spines (Urban-Ciecko and Barth, 2016), whose Ca^{2+} activities were suppressed after EA (Figure 3), we first examined the activity of SST-INs in S1 after transfecting Cre-dependent GCaMP6s into those cells (Figures 4A and 4B). The soma of SST-INs in CCI group presented lower total Ca^{2+} activities, which were enhanced by EA treatment (Figure 4C). Specifically, such modulation on total integrated Ca^{2+} activities (Figures 4D and 4E) were mainly attributed to the EA-induced re-elevation of peak values (Figures 4H and 4I) but not the frequency of Ca^{2+} spikes (Figures 4F and 4G). These results suggested that CCI leads to the inhibition of SST-INs soma, and EA treatment potentiates GABAergic transmissions.

We further tracked the activity of SST-INs axons, which form direct synaptic connections with apical spines of L5PNs (Urban-Ciecko and Barth, 2016). Similar phenotypes were identified by two-photon imaging, as total integrated Ca^{2+} activities and peak values, but not Ca^{2+} spike frequency, were remarkably inhibited

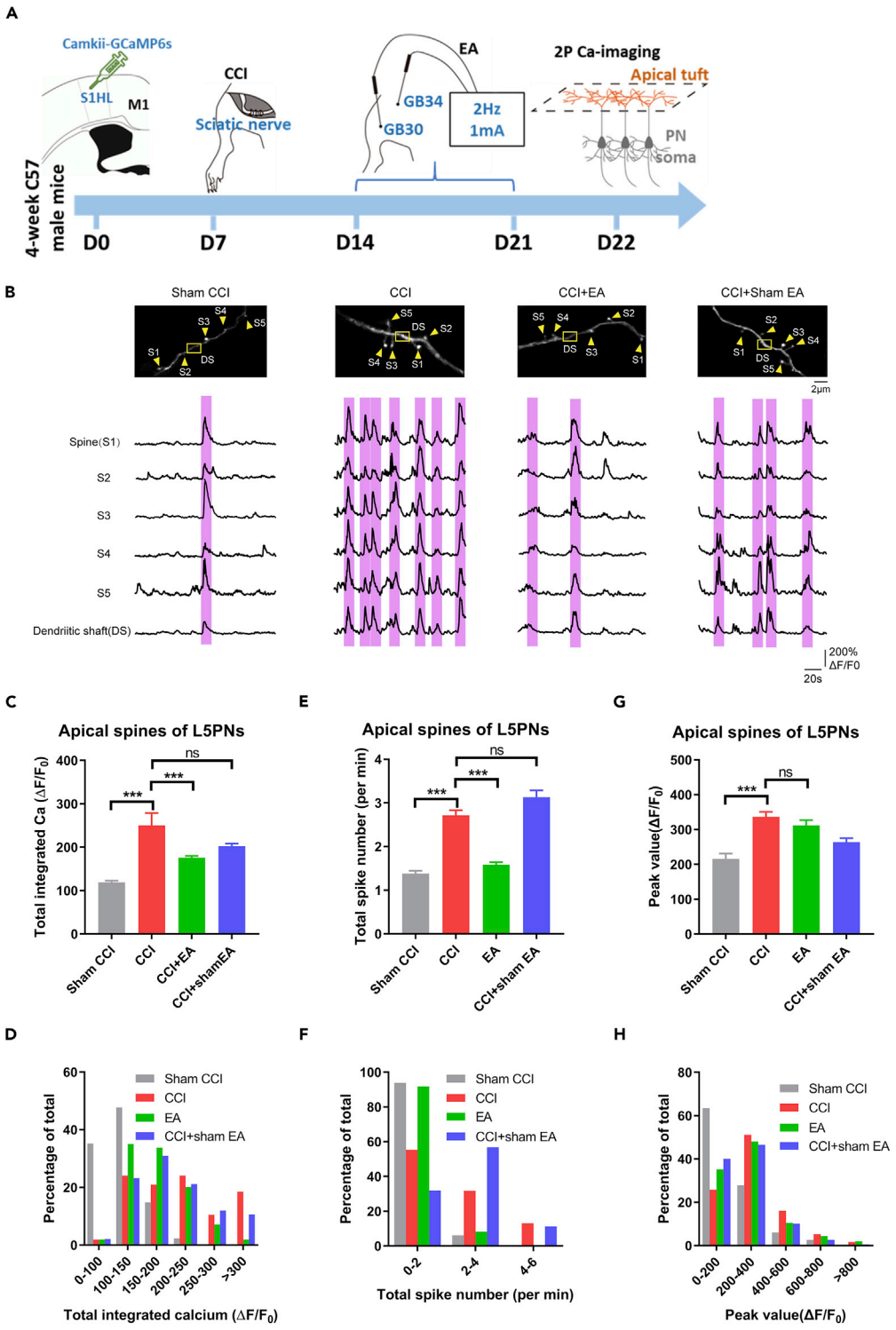

Figure 3. EA intervention modulates the activity of L5PN apical spines

(A) Schematic diagrams showing experimental timelines in (B–H), similar with those in Figure 2A.

(B) Top, representative apical dendrites (DS) and spines (S1 to S5) under two-photon imaging. Scale bar, 2 μm. Bottom, recording traces of Ca^{2+} activities after normalization ($\Delta F/F_0$). Pink shades indicate high levels of synchronization among spines on the same dendritic branch.

Figure 3. *Continued*

(C and D) Total integrated Ca^{2+} activities of apical spines. (C) Bar chart showing averaged total integrated Ca^{2+} activities (sham CCI: 118.9 ± 3.91, CCI: 250.3 ± 28.09, CCI + EA: 175.8 ± 4.13, CCI + sham EA: 202.1 ± 6.04; Kruskal-Wallis test statistic = 140.5, $p < 0.001$; ***$p < 0.001$ using Dunn's post-hoc comparison; ns, no significant difference; $n = 89$, 163, 167, and 151 spines, $N = 4$, 5, 6, and 4 animals for sham CCI, CCI, CCI + EA, and CCI + sham EA group, respectively). (D) The frequency distribution of total integrated Ca^{2+} activities.

(E and F) Spike numbers per minute of Ca^{2+} transients. (E) Averaged Ca^{2+} spike frequency (sham CCI: 1.38 ± 0.07, CCI: 2.71 ± 0.12, CCI + EA: 1.59 ± 0.05, CCI + sham EA: 3.13 ± 0.16; Kruskal-Wallis test statistic = 131.0, $p < 0.001$; ***$p < 0.001$ using Dunn's post-hoc comparison; ns, no significant difference; $n = 82$, 161, 158, and 116 spines, $N = 4$, 5, 6, and 4 animals for sham CCI, CCI, CCI + EA, and CCI + sham EA group, respectively). (F) The frequency distribution of Ca^{2+} spike frequency.

(G and H) Peak values of Ca^{2+} spikes. (G) Averaged Ca^{2+} peak values (sham CCI: 216.1 ± 15.01, CCI: 336.4 ± 14.52, CCI + EA: 312.1 ± 14.52 CCI + sham EA: 263.9 ± 11.19; Kruskal-Wallis test statistic = 46.66, $p < 0.001$; ***$p < 0.001$ using Dunn's post-hoc comparison; ns, no significant difference; $n = 100$, 201, 192, and 138 spines, $N = 4$, 5, 6, and 4 animals for sham CCI, CCI, CCI + EA, and CCI + sham EA group, respectively). (H) Histogram showing the frequency distribution of Ca^{2+} peak values. Data are presented as mean ± SEM.

in CCI group and were restored by EA treatment (Figure S5). The potentiated axonal Ca^{2+} activities indicate higher probability of GABA release at SST-PN synapse. These data agreed with previous reports (Cichon et al., 2017) by supporting a disinhibition of L5PNs under CCI, and further suggested that EA exerts its analgesic effects possibly by activating SST-INs to suppress PNs.

Within the local cortical circuit, vasoactive intestinal peptide-positive interneurons (VIP-INs) innervate SST-INs, adding one extra layer of activity regulation (Karnani et al., 2016). We next investigated if EA intervention also affected VIP-INs activities (Figures 5A and 5B). We found that VIP-INs displayed a similar phenotype as those in L5PNs: CCI remarkably potentiated their somatic Ca^{2+} activities, whereas EA treatment inhibited those neurons (Figure 5C). Total integrated Ca^{2+} activities (Figures 5D and 5E), Ca^{2+} spike frequencies (Figures 5F and 5G), and peak values (Figures 5H and 5I) were all increased in CCI model group and were depressed by EA intervention. We further recorded the activity of VIP-INs axons, which form synaptic connection with SST-INs (Karnani et al., 2016). Results showed similar patterns, in which the Ca^{2+} activity of VIP-IN axons was increased after CCI and was suppressed following EA intervention (Figures S6A–S6C). Such modulatory effects were mainly attributed to the changes of Ca^{2+} spike frequency but not peak values within the axonal region (Figures S6D–S6G), indicating potentiated GABA release at VIP-SST synapse. Taken together, both somatic and axonal data from cortical INs suggest a dual-layered modulation on cortical GABAergic activities, as EA treatment potentially suppresses VIP-INs, leading to the activation of SST-INs and the suppression of PNs as the consequence.

CB1R pathway underlies EA's modulation on cortical circuits and analgesia

After characterizing the cortical circuitry modulation by EA, we next explored the molecular mechanism. Using RNA sequencing to screen genes with differential expressions in S1 under both CCI and EA treatment, we adopted Kyoto Encyclopedia of Genes and Genomes database to analyze the functional clusters that were most significantly affected by EA. Results showed that the retrograde endocannabinoid signaling pathway was remarkably changed (Figure 6A). As the upstream regulator of this pathway, CB1R has been implicated in pain processing across cortical regions (Woodhams et al., 2017), and recent data also support the role of CB1R in midbrain nuclei for reversing pain hypersensitivity (Yuan et al., 2018). We thus investigated if CB1R plays a role in EA-mediated cortical circuitry modulation and relief of mechanical/thermal hypersensitivity induced by neuropathic pain. The immunostaining first revealed the expression of CB1R on somas and neurites of VIP-INs (Figure 6B). The protein quantification further showed that CCI treatment remarkably decreased CB1R levels in S1, whereas EA intervention elevated its expression level (Figures 6C and 6D). Those results converged to support a CB1R-induced neuromodulation on Ca^{2+} activities of VIP-INs and their downstream neurons.

As functional evidence, we further used one potent CB1R agonist, WIN55, to mimic the effect of EA in reducing mechanical hypersensitivity. In CCI model mice, a single intraperitoneal (i.p.) injection of WIN55 rapidly elevated the mechanical pain threshold within 20 min (Figures S7A and S7B). Furthermore, two-photon imaging found that WIN55 treatment suppressed both the peak value and the total integrated intensity of Ca^{2+} spikes (Figures S7C–S7I). Such phenotypes largely recapitulated the modulatory effect of EA on L5PNs activity (Figure 2), indicating the potential role of CB1R activation underlying EA's functions in reliving neuropathic pain.

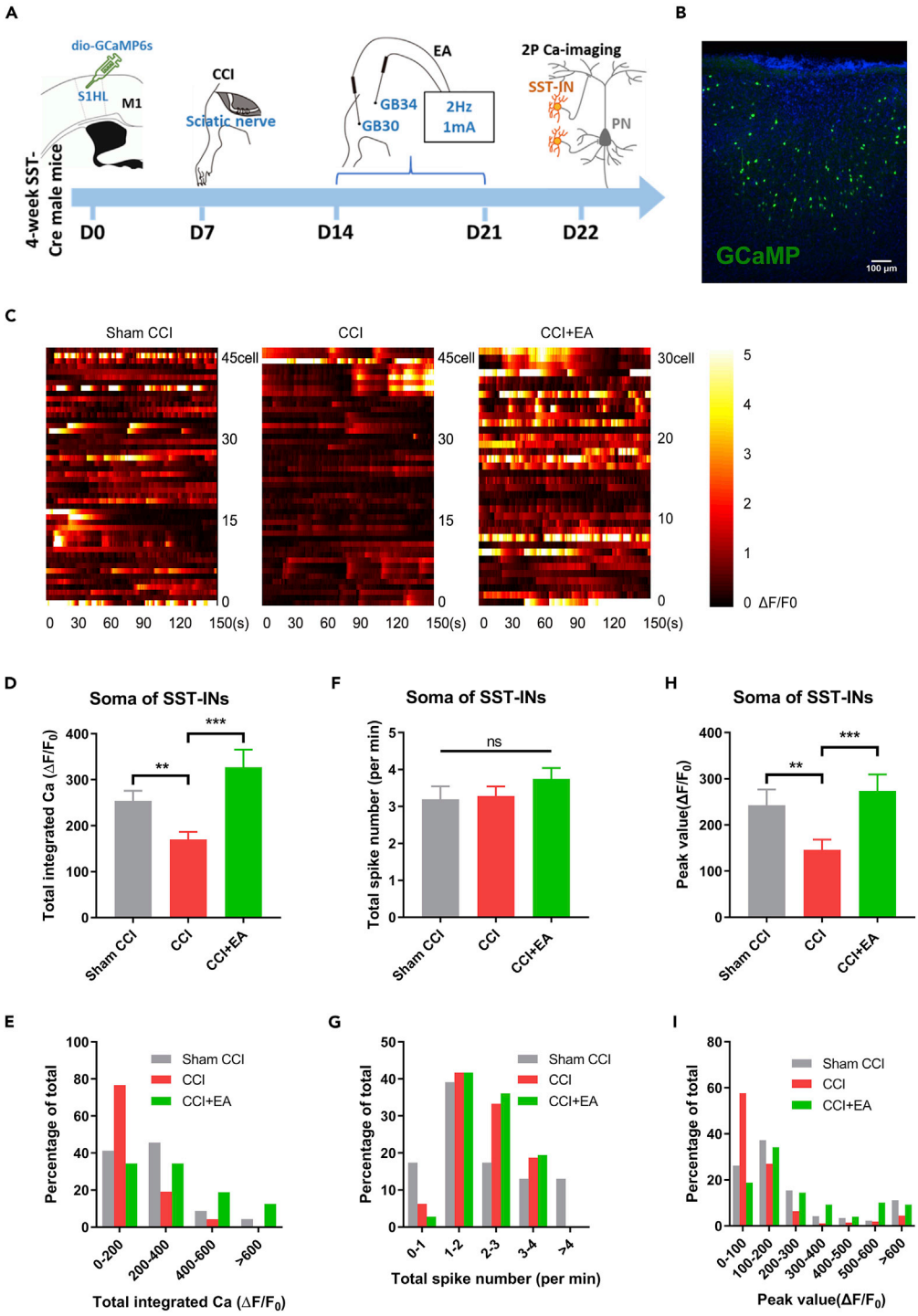

Figure 4. EA treatment potentiates somatostatin interneurons

(A) Experimental outlines in (C–I). Somatostatin (SST)-Cre mice received unilateral injection of AAV-dio-GCaMP6s virus into S1, followed by CCI surgery on D7 (contralateral side) and EA intervention. The activity of SST-interneurons (SST-INs) was recorded at the end of EA treatment (D22).

(B) Transfection sites of GCaMP6s. Scale bar, 100 μm.

(C) Heat maps showing normalized Ca^{2+} activities ($\Delta F/F_0$) of SST-INs soma during the 150-s recording period. A total of 45 representative cells were plotted for sham CCI and CCI group, and 30 representative cells were displayed for CCI + EA group.

Figure 4. *Continued*

(D and E) Total integrated Ca^{2+} activities in SST-INs soma. (D) Averaged total integrated Ca^{2+} activities (sham CCI: 254.3 ± 22.02, CCI: 170.0 ± 16.32, CCI + EA: 327.6 ± 38.03; Kruskal-Wallis test statistic = 19.09, $p < 0.001$; **$p = 0.0031$, ***$p < 0.001$ using Dunn's post-hoc comparison; $n = 63$, 59, and 45 neurons, $N = 4$, 5, and 5 animals for sham CCI, CCI, and CCI + EA group, respectively). (E) Histogram for the frequency distribution of total integrated Ca^{2+} activities.

(F and G) Ca^{2+} spike frequency (spike number per min) of SST-INs soma. (F) Averaged Ca^{2+} spike frequency (sham CCI: 3.19 ± 0.35, CCI: 3.28 ± 0.26, CCI + EA: 3.75 ± 0.30; ns, no significant difference from Kruskal-Wallis test; $n = 90$, 84, and 70 neurons, $N = 4$, 5, and 5 animals for sham CCI, CCI, and CCI + EA group, respectively). (G) Histogram showing the frequency distribution of Ca^{2+} spike frequency.

(H and I) Peak values of Ca^{2+} activities in SST-INs soma. (H) Averaged peak values of Ca^{2+} activities (sham CCI: 242.6 ± 34.38, CCI: 146.3 ± 21.88, CCI + EA: 273.5 ± 35.60; Kruskal-Wallis test statistic = 16.01, $p < 0.001$; **$p = 0.0079$, ***$p < 0.001$ using Dunn's post-hoc comparison; $n = 81$, 75, and 47 neurons, $N = 4$, 5, and 5 animals for sham CCI, CCI, and CCI + EA group, respectively). (I) Frequency distribution of peak values of Ca^{2+} activities. Data are presented as mean ± SEM.

To demonstrate the necessity of CB1R activation in the pain relief function of EA, we daily infused the CB1R antagonist, AM251, during 7-day persistent EA in CCI mice (Figure 6E). After systemic drug administration, EA + AM251-treated mice gradually displayed mechanical allodynia (Figure 6F), in association with both heat and cold hyperalgesia (Figures 6G–6I). These results demonstrated the abolishment of EA's analgesic functions after CB1R blockade, indicating the necessary role of CB1R. As neural circuitry evidence, *in vivo* Ca^{2+} imaging was performed on L5PNs after 7-day treatment of AM251 plus EA treatment (Figure 7A). Data analysis showed that whereas EA treatment remarkably decreased Ca^{2+} transients in CCI mice, AM251 administration re-elevated L5PNs activities (Figures 7B–7D). The treatment of AM251 remarkably increased Ca^{2+} peak values (Figures 7G and 7H) but not the frequency (Figures 7E and 7F), similar to those in CCI model mice (Figure 2). Last, we monitored if Ca^{2+} activities of SST-INs were modulated by AM251. A single i.p. injection of AM251 is sufficient to suppress the activity of SST-INs soma within 20 min on CCI mice receiving 7-day EA treatment (Figure S8), reversing EA-induced potentiation of Ca^{2+} peak values. Those pharmaceutical assays demonstrate that the activation of CB1R pathway is indispensable for EA-induced relief of cortical hyperactivity, and for its inhibition of mechanical/thermal hypersensitivity. In summary, our current study establishes a cortical mechanism in which EA treatment activates CB1R to suppress VIP-INs, leading to the disinhibition of downstream SST-INs and further inhibition of PNs, contributing to the relief of neuropathic pain.

DISCUSSION

To our knowledge, this study provides the first piece of *in vivo* evidence showing how the cortical circuit is modulated by repeated EA treatment to relieve neuropathic pain. Specifically, the activation of CB1R by EA leads to presynaptic inhibition at GABAergic VIP axonal terminals, resulting in the disinhibition of SST-INs and the suppression of L5PNs, and eventually reducing mechanical or thermal hypersensitivity. These results agree with previous findings reporting the dysregulation of cortical GABAergic transmission under neuropathic pain (Cichon et al., 2017) and identify CB1R as the mediator in restoring cortical E/I balance to ameliorate neuropathic pain after EA intervention.

The activity of L5PNs is closely correlated with perception threshold, and the manipulation of L5PNs can shift the sensory sensitivity (Takahashi et al., 2016). It is thus proposed that EA might modulate activities of L5PNs to improve pain hypersensitivity under neuropathic pain. Our results supported this model by showing the depression of *in vivo* Ca^{2+} activities of L5PNs after EA treatment, in association with the relief of pain behaviors. In particular, both apical spines and somas of L5PNs presented suppression of total Ca^{2+} activities, and apical spines had decreased frequency of Ca^{2+} spikes in EA treatment group (Figures 2 and 3), suggesting decreased pre-synaptic inputs under EA intervention. We thus examined the activity of inhibitory neural network because recent studies have reported the essential role of SST-INs in maintaining synaptic plasticity and neural functions (Chen et al., 2019; Adler et al., 2019). Here we found disinhibition of PNs as the result of suppressed inputs from SST-INs in CCI model as previously described (Cichon et al., 2017). More importantly, we identified the potentiation of SST-INs by EA treatment, which remarkably elevated the peak value of Ca^{2+} spikes in axonal regions (Figure S5), suggesting a higher probability of presynaptic GABAergic transmission for suppressing PN activities. Further analysis showed that VIP-INs are suppressed after EA treatment, providing a disinhibitory input for the projection from SST-IN to PN, and resulting in lower PN activities. These data collectively support the important role of E/I balance for maintaining cortical sensory function.

There are few studies regarding the molecular mechanism governing the cortical hyperactivity in neuropathic pain. The CB1R pathway has been widely accepted in pain processing (Woodhams et al., 2017).

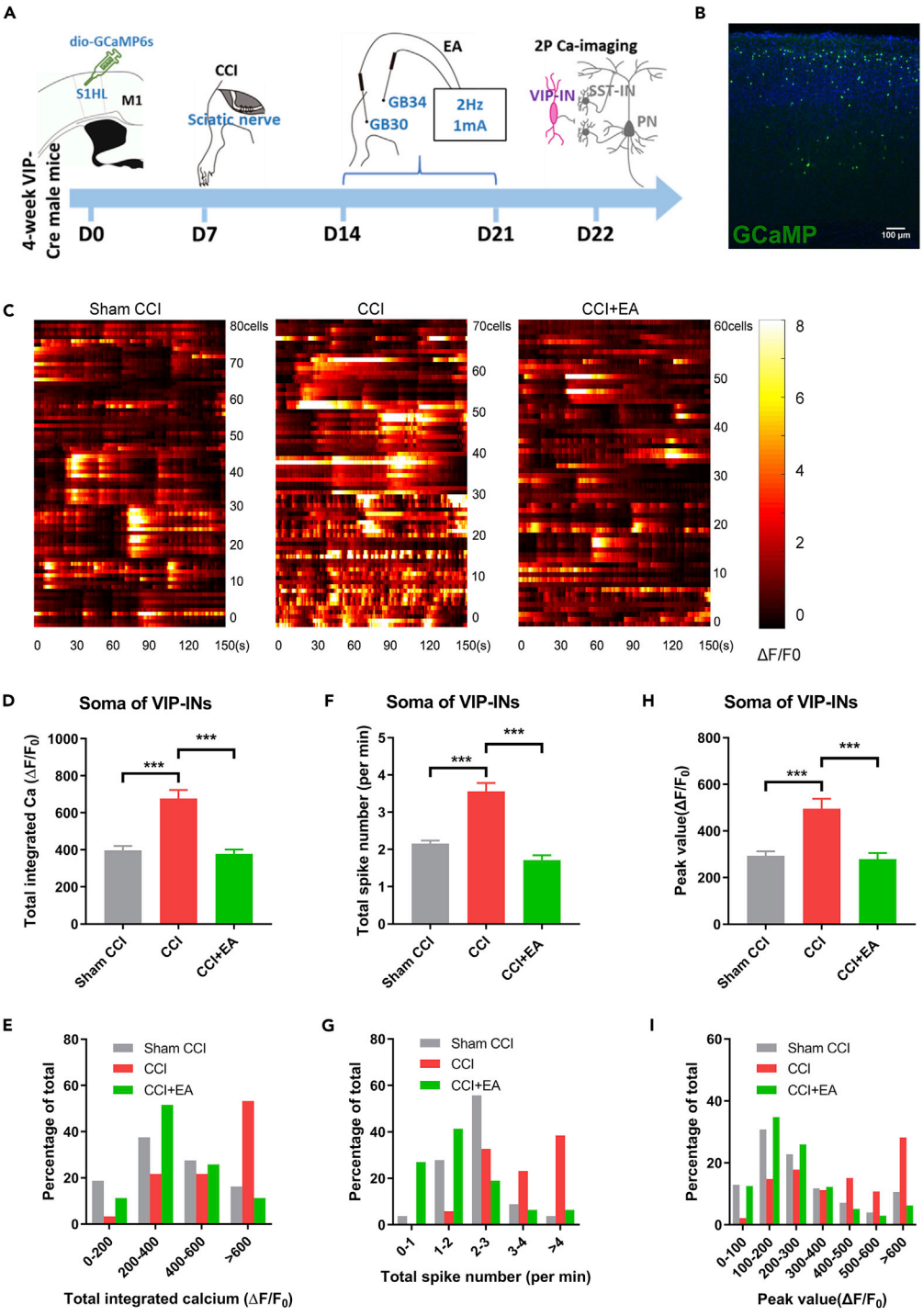

Figure 5. EA alleviates hyperactivation of vasoactive intestinal peptide-interneurons

(A) A brief experimental outline in C–I Vasoactive intestinal peptide (VIP)-Cre mice were unilaterally transfected with AAV-dio-GCaMP6s virus into S1, treated by CCI surgery on D7, and received EA intervention as previous experiments. The activity of VIP-interneurons (VIP-INs) was recorded at the end of EA treatment (D22).

(B) Transfection sites of GCaMP6s within S1. Scale bar, 100 μm.

(C) Heat maps for time series recording of normalized Ca^{2+} activities (in $\Delta F/F_0$) of VIP-INs soma. A total of 60–80 representative cells were plotted from each group and a 150-s recording period was adopted.

Figure 5. *Continued*

(D and E) Total integrated Ca^{2+} activities of VIP-INs soma. (D) A bar chart showing total integrated Ca^{2+} activities (sham CCI: 396.9 ± 23.22, CCI: 678.3 ± 44.26, CCI + EA: 377.8 ± 23.08; Kruskal-Wallis test statistic = 34.88, $p < 0.001$; ***$p < 0.001$ using Dunn's post-hoc comparison; $n = 87$, 69, and 72 neurons, $N = 4$, 5, and 4 animals for sham CCI, CCI and CCI + EA group, respectively). (E) Histogram showing the frequency distribution of total integrated Ca^{2+}.

(F and G) Ca^{2+} spike frequency (calculated as the spike number per min) of VIP-INs soma. (F) Averaged Ca^{2+} spike frequency (sham CCI: 2.15 ± 0.08, CCI: 3.56 ± 0.22, CCI + EA: 1.71 ± 0.13; Kruskal-Wallis test statistic = 56.89, $p < 0.001$; ***$p < 0.001$ using Dunn's post-hoc comparison; $n = 79$, 52, and 64 neurons, $N = 4$, 5, and 4 animals for sham CCI, CCI, and CCI + EA group, respectively). (G) The frequency distribution of Ca^{2+} spike frequency.

(H and I) Peak values of Ca^{2+} activities of VIP-INs soma. (H) Averaged peak values of Ca^{2+} activities (sham CCI: 292.8 ± 19.26, CCI: 495.8 ± 42.00, CCI + EA: 279.2 ± 26.09; Kruskal-Wallis test statistic = 23.56, $p < 0.001$; ***$p < 0.001$ using Dunn's post-hoc comparison; $n = 93$, 60, and 80 neurons, $N = 4$, 5, and 4 animals for sham CCI, CCI, and CCI + EA group, respectively). (I) Histogram showing the frequency distribution of peak values of Ca^{2+} spikes. Data are presented as mean ± SEM.

Across different brain regions including the spinal cord (Yang et al., 2016), midbrain nuclei (Walker et al., 1999), and prefrontal cortex (Huang et al., 2019), the activation of CB1R exerted analgesic effects. Our data suggest that CB1R activation is necessary for EA's analgesic effects. Although the pharmaceutical manipulation of CB1R cannot exclude its effect in midbrain regions as previously reported (Yuan et al., 2018; Shou et al., 2013; Chen et al., 2018), the Ca^{2+} recording data of cortical INs and PNs suggested that cortical CB1R might play a role in EA-induced analgesia.

One unanswered question is how EA treatment at two peripheral acupoints leads to CB1R potentiation. Two possibilities may exist: (1) EA facilitates the endocannabinoids release, leading to the up-regulation of CB1R, and (2) other peripheral or central factors are released upon EA intervention, indirectly resulting in CB1R activation. For the former model, previous study has found the increased release of anandamide in PAG after local electrical stimulation to relieve hyperalgesia (Walker et al., 1999). It is thus possible that sensory stimulation by EA results in cortical release of endocannabinoids. To support the latter model, one study reported an orexin-dependent release of 2-arachidonoylglycerol (2-AG) signaling to activate CB1R in the ventrolateral PAG after EA stimulation on the median nerve (Chen et al., 2018). In short, a cross talk may exist between different neuromodulators to affect synaptic plasticity across the whole pain regulatory network after EA stimulation.

Another major challenge for revealing the neural mechanism of EA exists in the identification of its primary functioning sites or brain regions. Different models have been raised involving the local acupoints, spinal cord, midbrain nuclei, and cortex. Previous studies suggested that the local activation of adenosine receptor mediates anti-nociceptive effects of acupuncture (Goldman et al., 2010). In the dorsal horn neurons of the spinal cord, the evoked response was reduced by EA treatment (Kim et al., 2011). Within the descending pathway, different midbrain nuclei such as nucleus raphe magnus, PAG, habenular nucleus, and arcuate nucleus have been implicated in EA-related analgesia (Zhao, 2008; Lee and Beitz, 1993; Chen et al., 2014). Across the neocortex, prefrontal region and anterior cingulate cortex have been correlated with EA (Ong et al., 2019; Chen et al., 2014). The current study dissected the cortical inhibitory network regulating PNs' output under EA intervention, to further emphasize the critical role of sensory cortex in EA's analgesia. As the higher sensory processing center, S1 neurons project to various cortical and subcortical nuclei. Recently, a CST pathway originating from S1 has been demonstrated to directly affect the plasticity of spinal dorsal horn INs, thus affecting the pain modulation (Liu et al., 2018). It is thus likely that the suppression of L5PNs by EA treatment modulates such CST-mediated descending pathway, affecting the pain gating in the spinal cord.

In sum, we have established a cortical neural circuit that helps to explain the effect of EA in reducing mechanical or thermal hypersensitivity under neuropathic pain. Such modulatory processes are dependent on CB1R activation, which leads to potentiated inhibitory inputs onto PNs of S1. Our data add further knowledge to the growing body of nociceptive circuits and provide more evidence for adopting acupuncture in clinical management of neuropathic pain.

Limitations of the study

The current study only described the modulation of local neural circuitry in the somatosensory cortex under EA intervention, leaving the changes in subcortical network largely unclear. Moreover, whether CB1R

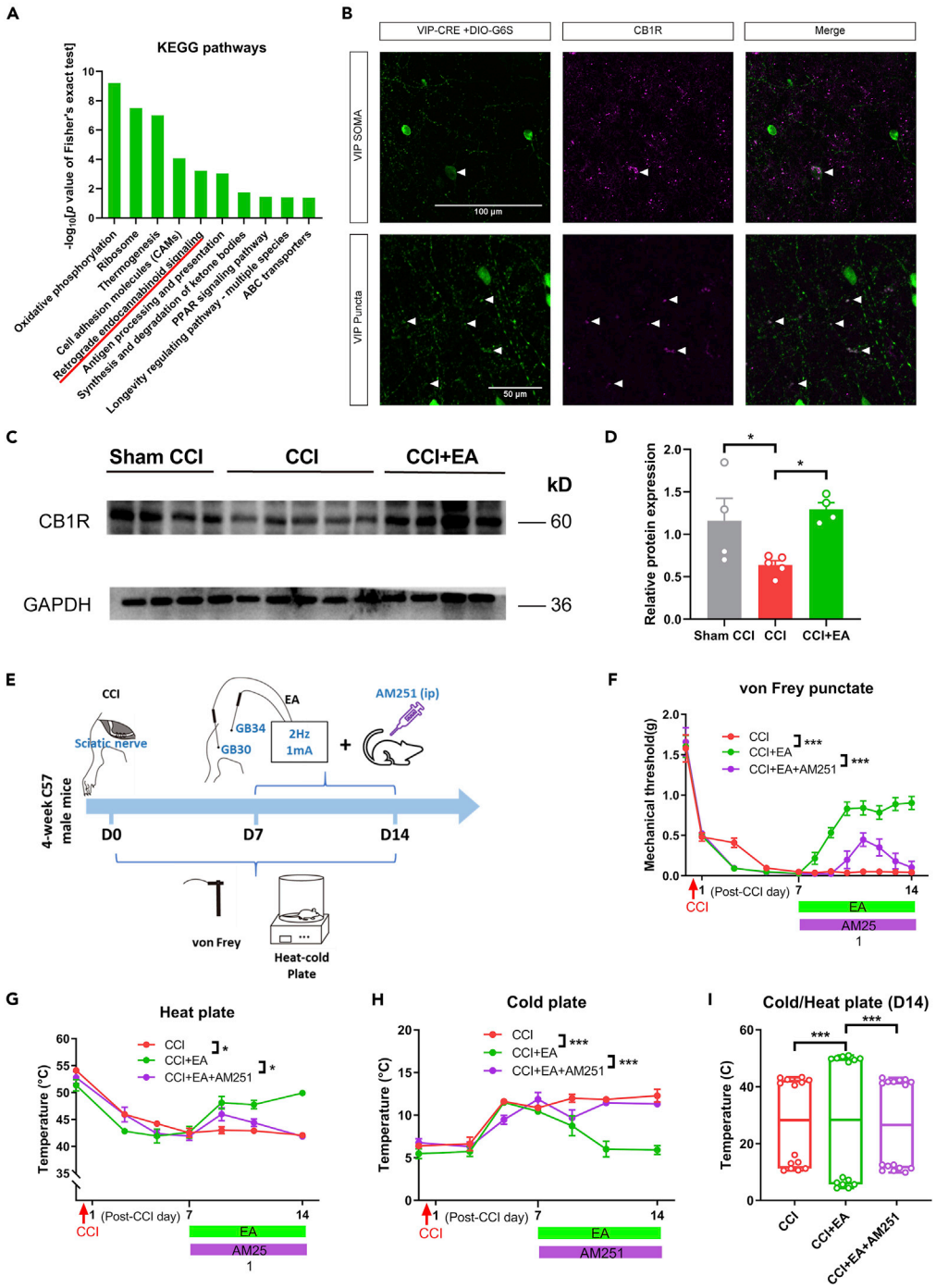

Figure 6. Endocannabinoid receptor 1 pathway underlies pain relief effects of EA

(A) Clustered enrichment of functional pathways based on RNA sequencing and Kyoto Encyclopedia of Genes and Genomes (KEGG) database.

(B) Immunostaining images showing the distribution of cannabinoid receptor 1 (CB1R) on VIP-INs soma (upper panels) and puncta (lower panels) in S1. Scale bar, 100 μm in upper panels; 50 μm in lower panels.

(C) Representative gel images from western blotting using CB1R-specific antibody and total protein extracts from S1.

(D) Relative protein expression levels of CB1R. One-way ANOVA: $F(2, 10) = 5.781$, $p = 0.0215$; *$p = 0.0421$ between sham CCI and CCI group; *$p = 0.0249$ between CCI and CCI + EA group using Tukey post-hoc test; $n = 4$, 5, and 4 animals from sham CCI, CCI, and CCI + EA group, respectively.

Figure 6. *Continued*
(E) Schematic diagram of CB1R blockade assay for (F–I). C57BL/6 mice received CCI surgery, and EA intervention was applied in conjunction with intraperitoneal (i.p.) infusion of AM251 for 7 days.
(F) Mechanical thresholds during 14-day CCI surgery and intervention (two-way ANOVA, group factor: $F(2, 240) = 94.92$, $p < 0.001$; ***$p < 0.001$ using Bonferroni post-hoc comparison; ns, no significant difference; $n = 7$, 10, and 6 animals for sham CCI, CCI + EA, and CCI + EA + AM251 group, respectively).
(G) Lowest temperature threshold on the heat plate (two-way ANOVA, group factor: $F(2, 114) = 5.688$, $p = 0.0116$; *$p = 0.0215$ between CCI and CCI + EA group; *$p = 0.0261$ between CCI + EA and CCI + EA + AM251 group using Bonferroni post-hoc comparison; $n = 7$, 7, and 8 animals for sham CCI, CCI + EA, and CCI + EA + AM251 group, respectively).
(H) Highest temperature threshold on the cold plate (two-way ANOVA, group factor: $F(2, 114) = 41.95$, $p < 0.001$; ***$p < 0.001$ using Bonferroni post-hoc comparison; $n = 7$, 7, and 8 animals for sham CCI, CCI + EA, and CCI + EA + AM251 group, respectively).
(I) Heat and cold threshold for each mouse in a single plotting (1-way ANOVA: $F(2, 19) = 160.4$, $p < 0.001$; ***$p < 0.001$ using Tukey post-hoc comparison; $n = 7$, 7, and 8 animals for sham CCI, CCI + EA, and CCI + EA + AM251 group, respectively). Data are presented as mean ± SEM.

mediates the pain-relieving effect via other brain regions or peripheral nerves is inconclusive based on current data.

Resource availability

Lead contact

Further information and requests for resources and reagents in this study can be fulfilled by contacting the Lead Contact, Li Zhang (zhangli@jnu.edu.cn).

Materials availability

This study did not generate new unique reagents.

Data and code availability

RNA sequencing data are available in the ArrayExpress database (http://www.ebi.ac.uk/arrayexpress) under accession number E-MTAB-9987.

METHODS

All methods can be found in the accompanying Transparent methods supplemental file.

SUPPLEMENTAL INFORMATION

Supplemental information can be found online at https://doi.org/10.1016/j.isci.2021.102066.

ACKNOWLEDGMENTS

We thank Dr. Yongjun Chen (Guangzhou University of Chinese Medicine) for the kind suggestions of the manuscript. The present study was supported by National Key Research and Development Program of China (2016YFC1306702) to K.-F.S. and L.Z., National Natural Science Foundation of China (81771455 and 81971067 to K.-F.S., 32070955 to L.Z., and 81973949 to M.L.), Outstanding Scholar Program of Guangzhou Regenerative Medicine and Health Guangdong Laboratory(2018GZR110102002) to K.-F.S. and L.Z., Science and Technology Program of Guangdong (2018B030334001) to K.-F.S., Science and Technology Program of Guangzhou, China (202007030012) to K.-F.S. and L.Z., and Guangdong Natural Science Foundation (2019A1515011772) to L.Z.

AUTHOR CONTRIBUTIONS

L.Z., X.H., and J.-a.W. conceived all experiments. X.H. generated CCI model and performed EA intervention. X.H., B.Z., and L.L. performed all behavioral, molecular, and immunofluorescent assays. J.W. performed two-photon calcium imaging assays with the help from K.C. and analyzed the imaging data. L.Z., M.L., and K.-F.S. supervised all experiments. L.Z., X.H., and J.-a.W. wrote the manuscript with feedback from all authors.

DECLARATION OF INTERESTS

The authors declare no conflict of interests.

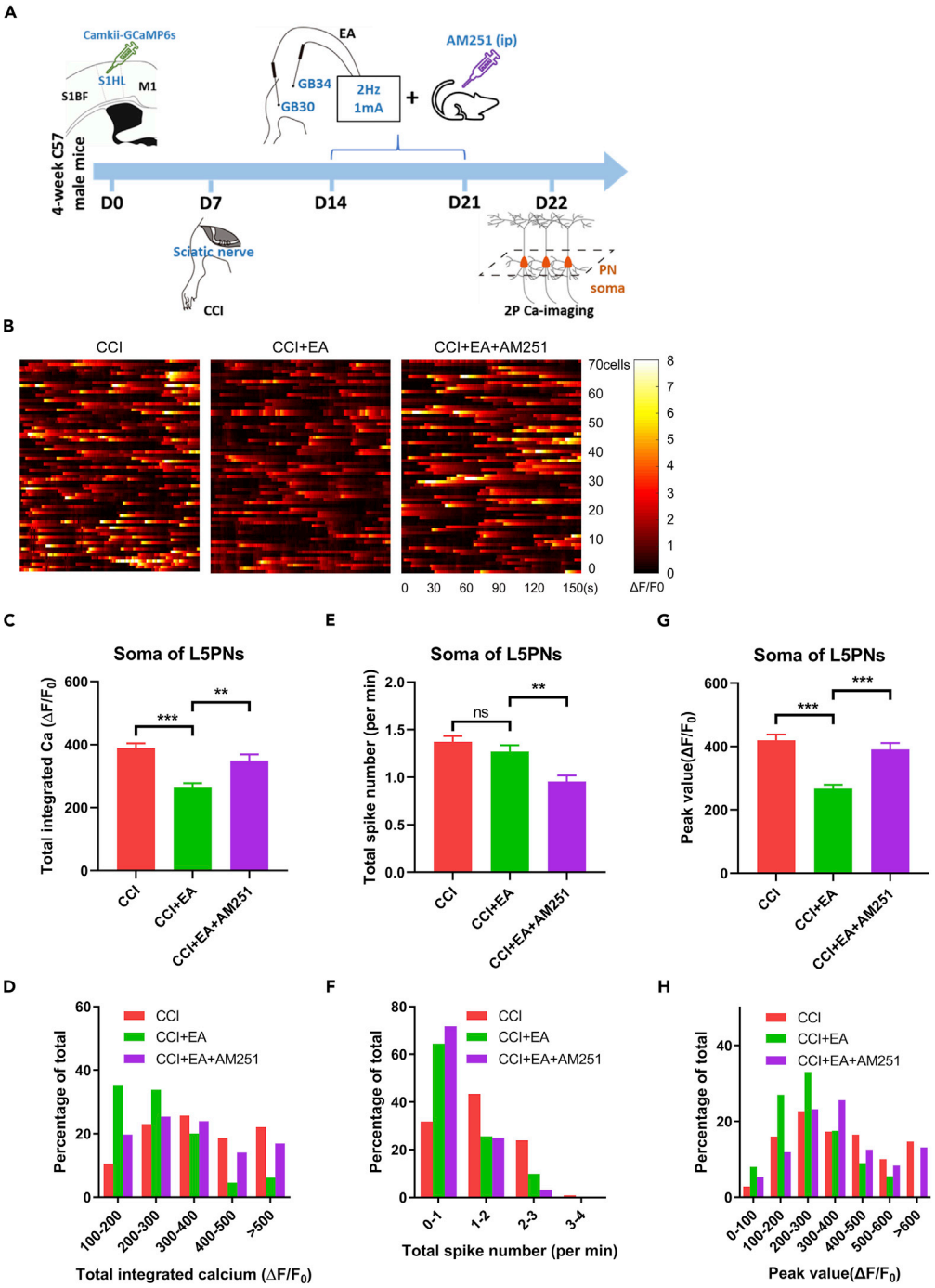

Figure 7. CB1R pathway is necessary for EA-repressed cortical hyperactivity

(A) Schematic diagram showing experimental timelines for (B to H). C57BL/6 mice received unilateral transfection of AAV-Camkii-GCaMP6s, and were treated with CCI surgery, plus EA intervention and 7-day i.p. infusion of AM251. On D22, two-photon imaging was performed on L5PNs in S1.

(B) Heat maps showing normalized Ca^{2+} activities of L5PNs. A total of 70 cells were plotted from each group with a recording duration of 150 s.

(C and D) Total integrated Ca^{2+} activities of L5PNs from CCI, CCI + EA, and CCI + EA + AM251 groups. (C) A bar chart showing averaged total integrated Ca^{2+} activities (CCI: 388.6 ± 15.46, CCI + EA: 263.7 ± 14.26, CCI + EA + AM251: 349.0 ± 19.85; Kruskal-Wallis test statistic = 28.25, $p < 0.001$; ***$p < 0.001$ between CCI and CCI + EA group; **$p = 0.0056$ between CCI + EA and CCI + EA + AM251 group using Dunn's post-hoc comparison; $n = 89$, 72, and 79 cells, $N = 4$, 5, and

Figure 7. *Continued*

4 animals for sham CCI, CCI + EA, and CCI + EA + AM251 group, respectively). (D) A histogram showing the frequency distribution of total integrated Ca^{2+} activities.

(E and F) Spike numbers per minute of Ca^{2+} transients on L5PNs. (E) A bar chart showing averaged Ca^{2+} spike frequency (CCI: 1.37 ± 0.06, CCI + EA: 1.27 ± 0.07, CCI + EA + AM251: 0.96 ± 0.06; Kruskal-Wallis test statistic = 19.84, $p < 0.001$; **$p = 0.0063$ between CCI + EA and CCI + EA + AM251 group; ns, no significant difference between CCI and CCI + EA group using Dunn's post-hoc comparison; $n = 83$, 64, and 70 cells, $N = 4$, 5, and 4 animals for sham CCI, CCI + EA, and CCI + EA + AM251 group, respectively). (F) The frequency distribution of Ca^{2+} spike frequency.

(G and H) Peak values of Ca^{2+} spikes. (G) Averaged Ca^{2+} peak values (CCI: 420.0 ± 17.81, CCI + EA: 267.1 ± 12.35, CCI + EA + AM251: 390.7 ± 20.76; Kruskal-Wallis test statistic = 33.82, $p < 0.001$; ***$p < 0.001$ using Dunn's post-hoc comparison; $n = 109$, 80, and 92 cells, $N = 4$, 5, and 4 animals for sham CCI, CCI + EA, and CCI + EA + AM251 group, respectively). (H) Histogram showing the frequency distribution of Ca^{2+} peak values. Data are presented as mean ± SEM.

Received: October 29, 2020
Revised: December 14, 2020
Accepted: January 11, 2021
Published: February 19, 2021

REFERENCES

Adler, A., Zhao, R., Shin, M.E., Yasuda, R., and Gan, W.B. (2019). Somatostatin-Expressing interneurons enable and maintain learning-dependent sequential activation of pyramidal neurons. Neuron *102*, 202–216.e7.

Alshelh, Z., Di Pietro, F., Youssef, A.M., Reeves, J.M., Macey, P.M., Vickers, E.R., Peck, C.C., Murray, G.M., and Henderson, L.A. (2016). Chronic neuropathic pain: it's about the rhythm. J. Neurosci. *36*, 1008–1018.

Aronoff, R., Matyas, F., Mateo, C., Ciron, C., Schneider, B., and Petersen, C.C. (2010). Long-range connectivity of mouse primary somatosensory barrel cortex. Eur. J. Neurosci. *31*, 2221–2233.

Bushnell, M.C., Duncan, G.H., Hofbauer, R.K., Ha, B., Chen, J.I., and Carrier, B. (1999). Pain perception: is there a role for primary somatosensory cortex? Proc. Natl. Acad. Sci. U S A *96*, 7705–7709.

Chen, K., Yang, G., So, K.F., and Zhang, L. (2019). Activation of cortical somatostatin interneurons rescues synapse loss and motor deficits after acute MPTP infusion. iScience *17*, 230–241.

Chen, X., Spaeth, R.B., Retzepi, K., Ott, D., and Kong, J. (2014). Acupuncture modulates cortical thickness and functional connectivity in knee osteoarthritis patients. Sci. Rep. *4*, 6482.

Chen, Y.H., Lee, H.J., Lee, M.T., Wu, Y.T., Lee, Y.H., Hwang, L.L., Hung, M.S., Zimmer, A., Mackie, K., and Chiou, L.C. (2018). Median nerve stimulation induces analgesia via orexin-initiated endocannabinoid disinhibition in the periaqueductal gray. Proc. Natl. Acad. Sci. U S A *115*, E10720–E10729.

Cichon, J., Blanck, T.J.J., Gan, W.B., and Yang, G. (2017). Activation of cortical somatostatin interneurons prevents the development of neuropathic pain. Nat. Neurosci. *20*, 1122–1132.

Clement-Jones, V., Mcloughlin, L., Tomlin, S., Besser, G.M., Rees, L.H., and Wen, H.L. (1980). Increased beta-endorphin but not met-enkephalin levels in human cerebrospinal fluid after acupuncture for recurrent pain. Lancet *2*, 946–949.

Eto, K., Ishibashi, H., Yoshimura, T., Watanabe, M., Miyamoto, A., Ikenaka, K., Moorhouse, A.J., and Nabekura, J. (2012). Enhanced GABAergic activity in the mouse primary somatosensory cortex is insufficient to alleviate chronic pain behavior with reduced expression of neuronal potassium-chloride cotransporter. J. Neurosci. *32*, 16552–16559.

Goldman, N., Chen, M., Fujita, T., Xu, Q., Peng, W., Liu, W., Jensen, T.K., Pei, Y., Wang, F., Han, X., et al. (2010). Adenosine A1 receptors mediate local anti-nociceptive effects of acupuncture. Nat. Neurosci. *13*, 883–888.

Guo, Z.L., Moazzami, A.R., and Longhurst, J.C. (2004). Electroacupuncture induces c-Fos expression in the rostral ventrolateral medulla and periaqueductal gray in cats: relation to opioid containing neurons. Brain Res. *1030*, 103–115.

Han, J.S. (2003). Acupuncture: neuropeptide release produced by electrical stimulation of different frequencies. Trends Neurosci. *26*, 17–22.

Harris, K.D., and Mrsic-Flogel, T.D. (2013). Cortical connectivity and sensory coding. Nature *503*, 51–58.

Hershman, D.L., Unger, J.M., Greenlee, H., Capodice, J.L., Lew, D.L., Darke, A.K., Kengla, A.T., Melnik, M.K., Jorgensen, C.W., Kreisle, W.H., et al. (2018). Effect of acupuncture vs sham acupuncture or waitlist control on joint pain related to aromatase inhibitors among women with early-stage breast cancer: a randomized clinical trial. JAMA *320*, 167–176.

Hinman, R.S., Mccrory, P., Pirotta, M., Relf, I., Forbes, A., Crossley, K.M., Williamson, E., Kyriakides, M., Novy, K., Metcalf, B.R., et al. (2014). Acupuncture for chronic knee pain: a randomized clinical trial. JAMA *312*, 1313–1322.

Ho, W.K., and Wen, H.L. (1989). Opioid-like activity in the cerebrospinal fluid of pain patients treated by electroacupuncture. Neuropharmacology *28*, 961–966.

Huang, J., Gadotti, V.M., Chen, L., Souza, I.A., Huang, S., Wang, D., Ramakrishnan, C., Deisseroth, K., Zhang, Z., and Zamponi, G.W. (2019). A neuronal circuit for activating descending modulation of neuropathic pain. Nat. Neurosci. *22*, 1659–1668.

Huang, Z.J., and Paul, A. (2019). The diversity of GABAergic neurons and neural communication elements. Nat. Rev. Neurosci. *20*, 563–572.

Jensen, T.S., and Finnerup, N.B. (2014). Allodynia and hyperalgesia in neuropathic pain: clinical manifestations and mechanisms. Lancet Neurol. *13*, 924–935.

Karnani, M.M., Jackson, J., Ayzenshtat, I., Hamzehei Sichani, A., Manoocheri, K., Kim, S., and Yuste, R. (2016). Opening holes in the blanket of inhibition: localized lateral disinhibition by VIP interneurons. J. Neurosci. *36*, 3471–3480.

Kim, H.Y., Wang, J., Lee, I., Kim, H.K., Chung, K., and Chung, J.M. (2009). Electroacupuncture suppresses capsaicin-induced secondary hyperalgesia through an endogenous spinal opioid mechanism. Pain *145*, 332–340.

Kim, J.H., Kim, H.Y., Chung, K., and Chung, J.M. (2011). Electroacupuncture reduces the evoked responses of the spinal dorsal horn neurons in ankle-sprained rats. J. Neurophysiol. *105*, 2050–2057.

Koo, S.T., Lim, K.S., Chung, K., Ju, H., and Chung, J.M. (2008). Electroacupuncture-induced analgesia in a rat model of ankle sprain pain is mediated by spinal alpha-adrenoceptors. Pain *135*, 11–19.

Lee, J.H., and Beitz, A.J. (1993). The distribution of brain-stem and spinal cord nuclei associated with different frequencies of electroacupuncture analgesia. Pain *52*, 11–28.

Liu, Y., Latremoliere, A., Li, X., Zhang, Z., Chen, M., Wang, X., Fang, C., Zhu, J., Alexandre, C., Gao, Z., et al. (2018). Touch and tactile neuropathic pain sensitivity are set by corticospinal projections. Nature *561*, 547–550.

Ma, S., Wu, J., Feng, Y., and Chen, B. (2011). Elevated estrogen receptor expression in hypothalamic preoptic area decreased by electroacupuncture in ovariectomized rats. Neurosci. Lett. *494*, 109–113.

MacPherson, H., Vertosick, E.A., Foster, N.E., Lewith, G., Linde, K., Sherman, K.J., Witt, C.M., and Vickers, A.J. (2017). The persistence of the effects of acupuncture after a course of treatment: a meta-analysis of patients with chronic pain. Pain *158*, 784–793.

Maeda, Y., Kim, H., Kettner, N., Kim, J., Cina, S., Malatesta, C., Gerber, J., Mcmanus, C., Ong-Sutherland, R., Mezzacappa, P., et al. (2017). Rewiring the primary somatosensory cortex in carpal tunnel syndrome with acupuncture. Brain *140*, 914–927.

Manns, I.D., Sakmann, B., and Brecht, M. (2004). Sub- and suprathreshold receptive field properties of pyramidal neurones in layers 5A and 5B of rat somatosensory barrel cortex. J. Physiol. *556*, 601–622.

Ong, W.Y., Stohler, C.S., and Herr, D.R. (2019). Role of the prefrontal cortex in pain processing. Mol. Neurobiol. *56*, 1137–1166.

Scarborough, B.M., and Smith, C.B. (2018). Optimal pain management for patients with cancer in the modern era. CA Cancer J. Clin. *68*, 182–196.

Shou, Y., Yang, Y., Xu, M.S., Zhao, Y.Q., Ge, L.B., and Zhang, B.M. (2013). Electroacupuncture inhibition of hyperalgesia in rats with adjuvant arthritis: involvement of cannabinoid receptor 1 and dopamine receptor subtypes in striatum. Evid. Based Complement. Alternat. Med. *2013*, 393460.

Takahashi, N., Oertner, T.G., Hegemann, P., and Larkum, M.E. (2016). Active cortical dendrites modulate perception. Science *354*, 1587–1590.

Ulett, G.A., Han, S., and Han, J.S. (1998). Electroacupuncture: mechanisms and clinical application. Biol. Psychiatry *44*, 129–138.

Urban-Ciecko, J., and Barth, A.L. (2016). Somatostatin-expressing neurons in cortical networks. Nat. Rev. Neurosci. *17*, 401–409.

Walker, J.M., Huang, S.M., Strangman, N.M., Tsou, K., and Sanudo-Pena, M.C. (1999). Pain modulation by release of the endogenous cannabinoid anandamide. Proc. Natl. Acad. Sci. U S A *96*, 12198–12203.

Witt, C., Brinkhaus, B., Jena, S., Linde, K., Streng, A., Wagenpfeil, S., Hummelsberger, J., Walther, H.U., Melchart, D., and Willich, S.N. (2005). Acupuncture in patients with osteoarthritis of the knee: a randomised trial. Lancet *366*, 136–143.

Woodhams, S.G., Chapman, V., Finn, D.P., Hohmann, A.G., and Neugebauer, V. (2017). The cannabinoid system and pain. Neuropharmacology *124*, 105–120.

Xing, G.G., Liu, F.Y., Qu, X.X., Han, J.S., and Wan, Y. (2007). Long-term synaptic plasticity in the spinal dorsal horn and its modulation by electroacupuncture in rats with neuropathic pain. Exp. Neurol. *208*, 323–332.

Yang, F., Xu, Q., Shu, B., Tiwari, V., He, S.Q., Vera-Portocarrero, L.P., Dong, X., Linderoth, B., Raja, S.N., Wang, Y., and Guan, Y. (2016). Activation of cannabinoid CB1 receptor contributes to suppression of spinal nociceptive transmission and inhibition of mechanical hypersensitivity by Abeta-fiber stimulation. Pain *157*, 2582–2593.

Yuan, X.C., Zhu, B., Jing, X.H., Xiong, L.Z., Wu, C.H., Gao, F., Li, H.P., Xiang, H.C., Zhu, H., Zhou, B., et al. (2018). Electroacupuncture potentiates cannabinoid receptor-mediated descending inhibitory control in a mouse model of knee osteoarthritis. Front Mol. Neurosci. *11*, 112.

Zhang, R., Lao, L., Ren, K., and Berman, B.M. (2014). Mechanisms of acupuncture-electroacupuncture on persistent pain. Anesthesiology *120*, 482–503.

Zhang, Y., Meng, X., Li, A., Xin, J., Berman, B.M., Lao, L., Tan, M., Ren, K., and Zhang, R.X. (2012). Electroacupuncture alleviates affective pain in an inflammatory pain rat model. Eur. J. Pain *16*, 170–181.

Zhao, Z.Q. (2008). Neural mechanism underlying acupuncture analgesia. Prog. Neurobiol. *85*, 355–375.

iScience, Volume *24*

Supplemental Information

Electroacupuncture activates inhibitory neural circuits in the somatosensory cortex to relieve neuropathic pain

Ji-an Wei, Xuefei Hu, Borui Zhang, Linglin Liu, Kai Chen, Kwok-Fai So, Man Li, and Li Zhang

Transparent Methods

Experimental animals

Male C57BL/6J mice (4 weeks old) were purchased from Guangdong Medical Laboratory Animal Center and were used for chronic constriction injury (CCI) model, behavioral assays, immunofluorescent staining, Western blot assay, virus injection and *in vivo* calcium recording. Male VIP-Cre and SST-Cre transgenic mice (4 weeks old) were obtained from the Jackson Laboratory (Bar Harbor, ME) and were bred in-house. All the animals were group-housed under normal light–dark cycle (0700-1900 on light) with food and water *ad libitum*. AM251 (MCE, HY-15443, 5 mg/kg) or WIN55(MCE, HY-13291, 2.5 mg/kg) was administered via intraperitoneal (ip) injection. In the acute pharmacological assay, behavioral test or *in vivo* calcium imaging was performed before and 20 min after drug infusion. Detailed information about grouping and timelines of each experiment can be found in Figs 1-7. All experimental protocols have been pre-approved by the Laboratory Animal Ethics Committee at Jinan University in accordance with National Guidance for Animal Experiment.

CCI model preparation

Chronic constriction injury (CCI) was adopted as previously described (Ong et al., 2019). In brief, mice were anaesthetized with 1.25% Avertin and the left sciatic nerve was exposed at the mid-thigh site with proximity to the sciatic trifurcation. After bluntly dissected the sciatic nerve from adjacent tissues, two catgut ligations were loosely tied around the nerve. Mice in the sham teams were anesthetized and were exposed for the left sciatic nerve using the same procedure but without the ligation.

EA intervention

Seven days after the CCI treatment, the mouse received daily EA (on 9~10 am) on two acupoints: Huantiao (GB30) and Yanglingquan (GB34), which have been demonstrated to be effective in relieving neuropathic pain (Wu et al., 2013). The EA sessions lasted for 7 days (from D8 to D14). In each treatment course, 2 acupuncture needles were inserted into designed acupoints with 2-3mm depth. The pulsed current (1 mA and 0.1 ms duration) was applied at 2 Hz for 30 min using a customized Acupoint Nerve Stimulator as previously described (Wu et al., 2013). In the sham EA group, the needles were inserted into skins at 2~3 mm adjacent to the acupoints.

Behavioral tests

All behavioral assays were performed at 6~8 hrs after EA stimulus.

Open field test. The mice were firstly habituated for 15 min in the test room. The mouse was put into a transparent box (50 cm × 50 cm) for freely moving during a single 6 min test session. An infrared digital camera was used to track the animal movements. Ethovison XT version 3.0 software (Noldus, Wageningen, The Netherlands) was applied to analyze the time duration in central zone (25 cm × 25 cm), in addition to total distance and mean velocity.

Mechanical allodynia assay. Mechanical allodynia was measured with a series of von Frey filaments (0.008, 0.02, 0.04, 0.07, 0.16, 0.4, 0.6, 1.0, 1.4, and 2.0 g; 2.0 g cutoff) as previously described (Alba-Delgado et al., 2018). Three days before the first test, mice were habituated in the test room for measuring the basal level of mechanical threshold.

Acetone test. The mouse was put on the top of a wire mesh, with a drop (100 ul) of acetone into the

middle surface of its hind-paw. Animal responses were watched for 1 min after acetone application and were graded based on a 0-3 scale as described previously (Flatters and Bennett, 2004): 0, no response; 1, quick withdrawal, flick or stamp of the paw; 2, prolonged withdrawal or repeated flicking of the paw; 3, repeated flicking of the paw with persistent licking directed at the ventral side of the paw. In general, a total of 3 acetone drops were applied with a 5 min time interval between each session, and averaged scores were calculated for each mouse.

Hot/cold plate. The animals were placed on a metal plate (275 mm × 263 mm × 15 mm). The assay was initiated from 5 min acclimation at 30 ℃. The temperature was increased or decreased at a rate of 6℃ min^{-1} velocity until the mouse manifested aversive behaviors, including hind-paw licking, shaking, lifting or jumping. The plate temperature at which any of above responses occurred was defined as the heat/cold threshold. Each animal was tested twice per day for calculating the average data.

Stereotaxic injection

Four-week old WT mice were anesthetized with 1.25% Avertin. After making an incision on the scalp and local sterilization, the periosteum tissue was removed. The hindlimb region of primary somatosensory cortex (S1HL, -0.5 mm anterior to the Bregma and 1.5 mm lateral) was located by a stereotaxic instrument (RWD, China). An injection hole was made on the skull by a high-speed micro-drill (OmniDrill35, WPI, USA), and a total 80nl of AAV2/1-hSyn-GCaMP6s (>1×10^{13} gene copies/ml, provided by the University of Pennsylvania Gene Therapy Program Vector Core) was injected into the cortical layer 5 using a glass microelectrode connected with an ultra-micro injection pump (Nanoliter 2010, WPI, USA) in a 60^{o} angle to avoid the damage of the imaging site.

Alternatively, 150nl of AAV2/1-hSyn-DIO-GCaMP6s (>1 × 10^{13} gene copies/ml, the University of Pennsylvania Gene Therapy Program Vector Core) was injection into S1HL of VIP-Cre mice and SST-Cre mice. The glass electrode was retained in the brain tissue for 5 min before retraction. All the *in vivo* calcium image was performed 3 weeks after injection.

***In vivo* calcium imaging**

After recovery from the stereotaxic injection, the mice were used to perform *in vivo* calcium image under awake, head-restrained condition. The mice were anesthetized with 1.25% Avertin, then the scalp was removed to expose the skull. After leaning the surface of skull, two metal bars were attached to the rostral and caudal skull with glue (Loctite 401), dental cement was then applied surrounding the imaging region to fix the metal bars. On the next day, an imaging window above SIHL was created by a high-speed micro-drill, and was cover by a glass coverslip using Vetbond Tissue Adhesive (3M, USA). The imaging session was performed using 920 nm excitation laser with a water-immersed objective (20×, 1.1 numerical aperture; ZEISS, Germany). The calcium activities of apical tufts (0-80 μm from pia), L5PN somas (600-650 μm from pia), SST somas and axons (400-500 μm from pia) and VIP somas and axons (200-300 μm from pia) were recorded at 2 Hz during a 2.5-min period using an LSM780 two-photon microscope (ZEISS, Germany)

Time-series images of calcium signals were corrected by TurboReg plugin of ImageJ (Bethesda, MD, US). Regions of interest (ROIs) were manual designed for somas, apical spines or axons. The fluorescent value (F) was averaged from mean pixels. Normalized fluorescent values ($\Delta F/F_0$) was calculated as $(F-F_0)/F_0$, where F_0 (baseline level) was the averaged F values during the first 10% of the recording period. The total integrated calcium value was the sum of $\Delta F/F_0$ during the 2.5 min

time series. A calcium spike was defined as the increase of three-folds or higher of standard deviations (SD) of whole recording session.

Transcriptome sequencing

Total RNA was isolated and purified from mouse S1 tissues using TRIzol reagent (Invitrogen, Carlsbad, CA, USA) following the manual instruction. RNA quality and concentration were determined by NanoDrop ND-1000 (NanoDrop, Wilmington, DE, USA). Poly (A) RNA was purified using poly-T oligo-attached magnetic microbeads, and was fragmented under high temperature. *In vitro* reverse transcription was adopted to prepare cDNA library using mRNASeq sample preparation kit (illumine, San Diego, CA, USA). The sequencing was performed on IlluminaHiSeq 4000 (LC Science, USA). Reads quality was assessed by FastQC (v.0.10.1). All reads were aligned to a reference genome of mouse using Hisat (v.2.0), and were assembled using StringTie (v.1.3.0). After the generation of final transcriptome, mRNA expression levels were calculated as fragments per kilobase per million reads (FPKM) using StringTie. Differential expression of mRNAs was identified by edgeR. Those mRNAs having differential expressions with statistical significance (p value < 0.05) in both sham CCI vs CCI and CCI vs CCI + EA comparison pairs were identified. Further functional enrichment of cellular pathway clusters was analyzed using KEGG database (http://www.kegg.jp/kegg).

Western blotting

Brain tissues were extracted from S1HL regions on the contralateral side of CCI after euthanized. Proteins concentration was quantified by BCA reagent (Beyotime, Shanghai, China). A total of 8 μg

protein samples were separated in 10% polyacrylamide gel electrophoresis under 110 V electrical field for 60 min, and were transferred to polyvinylidene fluoride (PVDF) membrane (Pall Life Science, Port Washington, NY, USA) using a 200 mA electrical current for 60 min. The membrane was blocked for 1 h using 5% BSA blocking buffer, and then was incubated with primary antibody at 4°C for 16 h. After washing, the membrane was incubated in secondary antibody for 1 h at room temperature. The membrane was developed in ECL chromogenic substrates, and an automatic protein imaging system (Bio-Rad, Hercules, CA, USA) was used to visualize protein bands. Optical density values of each band were measured by image J software (NIH, Bethesda, MD, USA). Relative protein expression was normalized to that of GAPDH. Primary and secondary antibody used are listed in table S2.

Tissue preparation and immunofluorescent staining

Animals were deeply anesthetized with 1.25% Avertin and perfused with 0.01M phosphate-buffered saline (PBS) followed by 4% paraformaldehyde (PFA). The whole brain was quickly removed and fixed overnight in 4% PFA at 4 °C, and was dehydrated in 30% sucrose. The brains were sectioned into 40 μm coronal slices by a sliding microtome (Leica, Germany). Brain slices were washed in PBS, and were blocked by CAS-Block buffer (Thermo Fisher Scientific, USA) containing 0.3% Triton X-100 for 1h at room temperature. The primary antibody was then applied for 48-hour incubation. After further incubation in the secondary antibody diluents, images were captured by a confocal microscope (ZEISS, Germany), and were analyzed by ImageJ. Primary and secondary antibody used are listed in table S1.

For the quantification of cFos, tissue harvest and fixation were performed at 24 hr after EA

stimulation. A total of 3 consecutive coronal slices were extracted from each mouse, and the number of cFos+ cells were averaged. The animal number ranged between 5 and 9 across different groups (see legends of Fig. S2 and S4). For the ease of counting, a 20X magnification field (512×512 pixels with 0.6μm pixel volume) was adopted from the contralateral side of CCI.

Statistical analysis

All data were presented as mean±standard error of means (s.e.m.), unless otherwise specified. Each dataset was first tested for normality (Gaussian distribution), as those data fitted the normal distribution were enrolled for parametric analysis. Student *t*-test was employed for comparison between two groups, and one-way analysis of variance (ANOVA) was used when comparing among multiple groups, followed by Tukey post-hoc comparison between 2 specified groups. Two-way ANOVA was adopted when 2 variables were simultaneously considered, followed by Bonferroni post-hoc comparison. When data were not fitted for normal distribution, non-parametric assays were adopted. In specific, Wilcoxon matched-pair test was used for paired comparison; and Kruskal-Wallis test was used for multi-group comparison, followed by Dunn's post-hoc comparison between 2 specified groups. GraphPad Prism ver 7.0 package (GraphPad Inc, USA) was used for statical analysis and data plotting.

References:

ALBA-DELGADO, C., MOUNTADEM, S., MERMET-JORET, N., MONCONDUIT, L., DALLEL, R., ARTOLA, A. & ANTRI, M. 2018. 5-HT(2A) Receptor-Induced Morphological Reorganization of PKCγ-Expressing Interneurons Gates Inflammatory Mechanical Allodynia in Rat. *The Journal of neuroscience : the official journal of the Society for Neuroscience,* 38**,** 10489-10504.

FLATTERS, S. J. & BENNETT, G. J. 2004. Ethosuximide reverses paclitaxel- and vincristine-induced painful peripheral neuropathy. *Pain,* 109**,** 150-61.

ONG, W. Y., STOHLER, C. S. & HERR, D. R. 2019. Role of the Prefrontal Cortex in Pain Processing.

Mol Neurobiol, 56**,** 1137-1166.

WU, C. H., LV, Z. T., ZHAO, Y., GAO, Y., LI, J. Q., GAO, F., MENG, X. F., TIAN, B., SHI, J., PAN, H. L. & LI, M. 2013. Electroacupuncture improves thermal and mechanical sensitivities in a rat model of postherpetic neuralgia. *Mol Pain,* 9**,** 18.

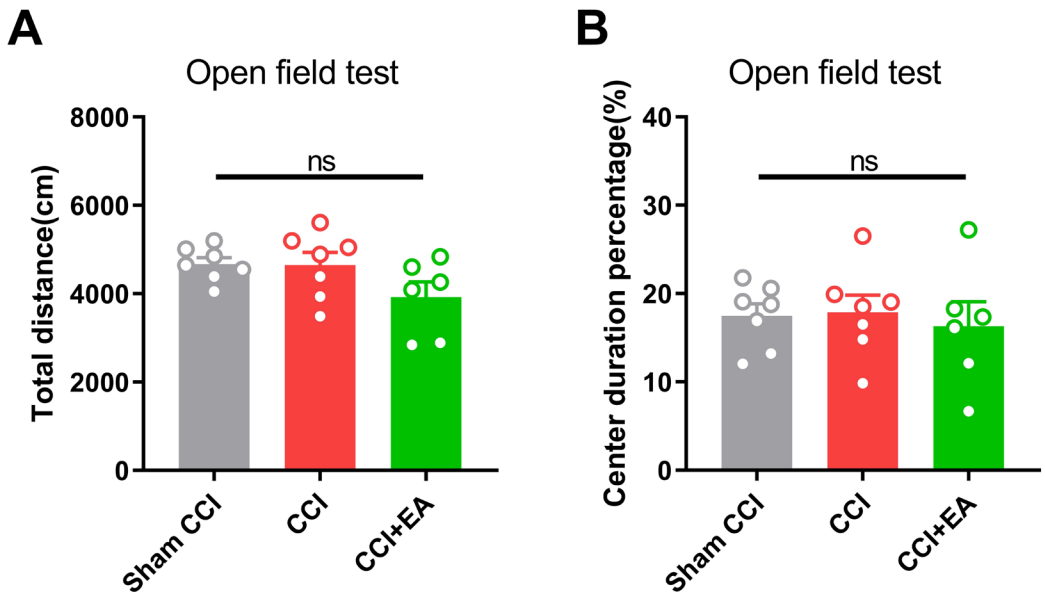

Fig. S1. General activity of CCI and EA treated mice, Related to Figure 1. (**A**) unchanged total distance (in cm) of mice in the open field. (**B**) no change of central zone duration across all groups. ns, no significant difference using Tukey's post-hoc comparison following one-way ANOVA. *n*=7, 7 and 5 for sham CCI, CCI and CCI+EA group, respectively. Data are presented as mean±SEM.

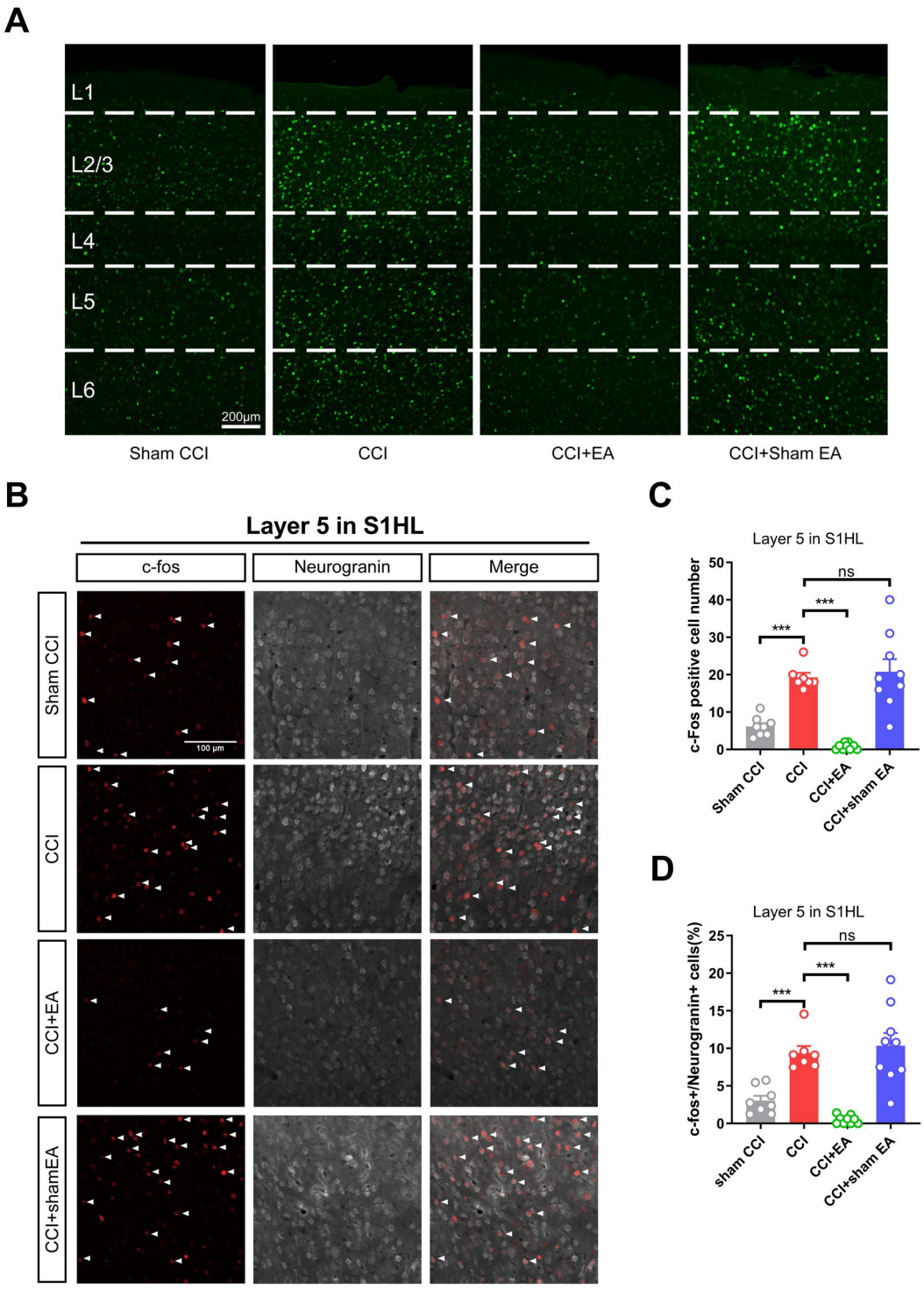

Fig. S2. Inactivation of cortical excitatory neurons by EA intervention, Related to Figure 2.

(**A**) A panoramic view of c-Fos staining in S1. Scale bar, 200 μm. (**B**) c-Fos staining of cortical neurons in S1 (left), plus merging with neurogranin (middle and right). Scale bar, 100 μm. (**C**) CCI model presented more c-Fos positive cells in layer 5 of hindlimb region of primary somatosensory

cortex (S1HL), and EA treatment suppressed c-Fos activation (1-way ANOVA, $F(3, 29)=25.75$, $P<0.001$; ***$P<0.001$ using Tukey post-hoc comparison; ns, no significant difference; $n=8, 7, 9$ and 9 animals for sham CCI, CCI, CCI+EA and CCI+sham EA group, respectively). (**D**) CCI group presented a higher fraction of c-Fos positive cells among excitatory (Neurogranin+) cells, and EA treatment deactivated those cells (1-way ANOVA, $F(3, 29)=21.42$, $P<0.001$; ***$P<0.001$ using Tukey post-hoc comparison; ns, no significant difference; $n=8, 7, 9$ and 9 animals for sham CCI, CCI, CCI+EA and CCI+sham EA group, respectively). Data are presented as mean±SEM.

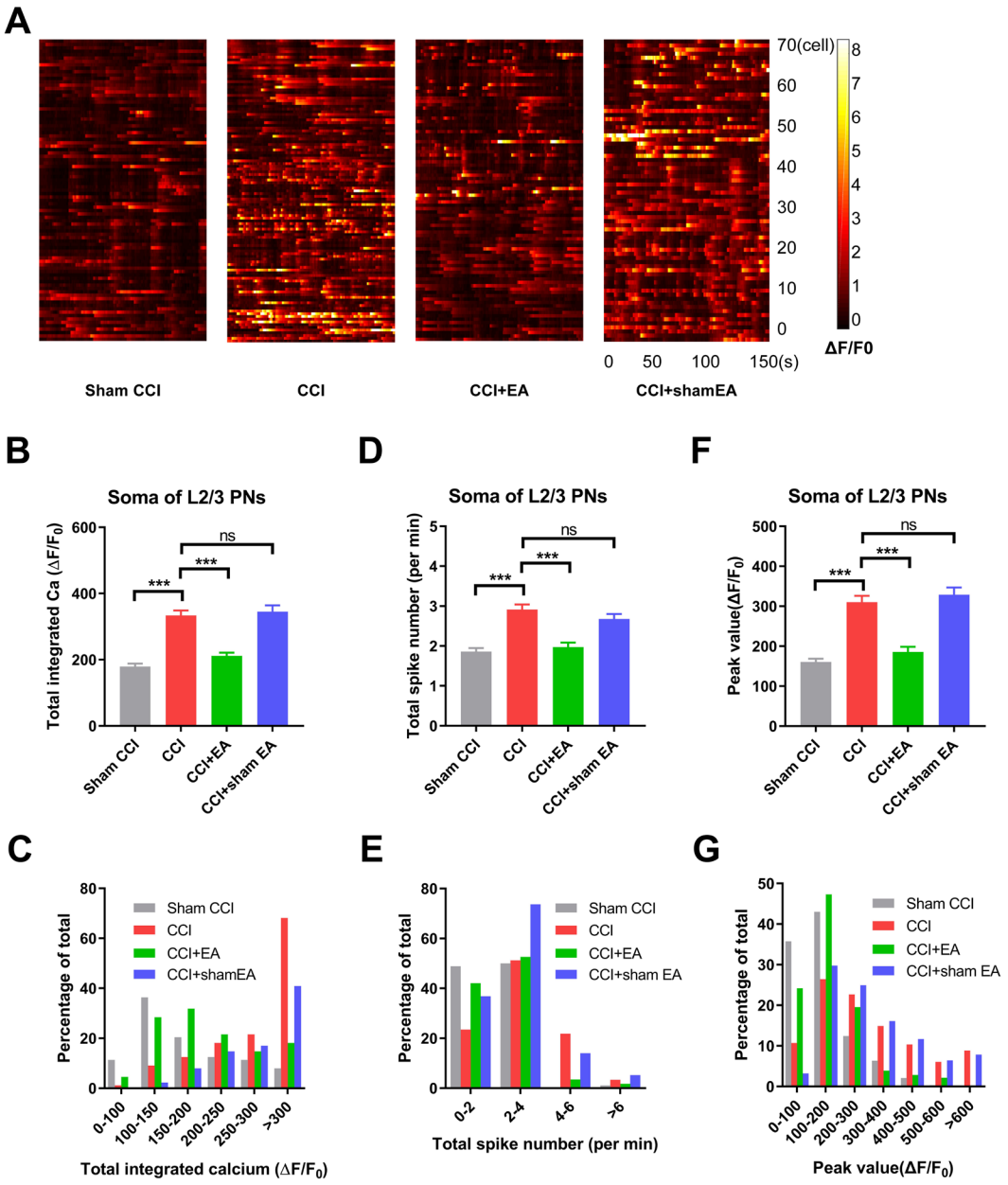

Fig. S3. EA relieves the hyperactivity of L2/3 PNs in CCI mice, Related to Figure 2. (**A**) Time-series heat maps showing Ca^{2+} activities of L2/3 PNs during a 150s recording window. Raw data have been normalized against the resting level ($\Delta F/F_0$). A total of 70 representative neurons were plotted in each group. (**B** to **C**) Total integrated Ca^{2+} activities of L2/3 PNs. Top (**B**), CCI elevated averaged total integrated Ca^{2+} activities, whilst EA suppressed the neuronal activation (sham CCI: 179.3±8.96, CCI: 333.8±14.73, CCI+EA: 211.9±9.19, CCI+Sham EA: 345.4±18.99; Kruskal-Wallis

test statistic=114.4, $P<0.001$; ***$P<0.001$ using Dunn's post-hoc comparison; n=89, 117, 106 and 74 neurons, N=4, 5, 5 and 4 animals for sham CCI, CCI, CCI+EA and CCI+sham EA group, respectively). Bottom (**C**), histogram for the frequency distribution of total integrated Ca^{2+} activities. (**D** to **E**) Ca^{2+} spike frequency (spike number per min) of L2/3 PNs was potentiated by CCI and was inhibited by EA. Top (**D**), averaged Ca^{2+} spike frequency (sham CCI: 1.86±0.09, CCI: 2.91±0.13, CCI+EA: 1.97±0.11, CCI+Sham EA: 2.68±0.12; Kruskal-Wallis test statistic=46.94, $P<0.001$; ***$P<0.001$ using Dunn's post-hoc comparison; n=90, 117, 74 and 77 neurons, N=4, 5, 5 and 4 animals for sham CCI, CCI, CCI+EA and CCI+sham EA group, respectively). Bottom (**E**), histogram showing the frequency distribution of Ca^{2+} spike frequency. (**F** to **G**) Peak values of Ca^{2+} activities were also increased by CCI, and were down-regulated with EA intervention. Top (**F**), averaged peak values of Ca^{2+} activities (sham CCI: 160.6±7.87, CCI: 310.3±15.77, CCI+EA: 185.5±12.86, CCI+Sham EA: 329.0±17.79; Kruskal-Wallis test statistic=98.83, $P<0.001$; ***$P<0.001$ using Dunn's post-hoc comparison; n=81, 75 and 47 neurons, N=4, 5 and 5 animals for sham CCI, CCI and CCI+EA group, respectively). Bottom (**G**), frequency distribution of peak values of Ca^{2+} activities. Data are presented as mean±SEM.

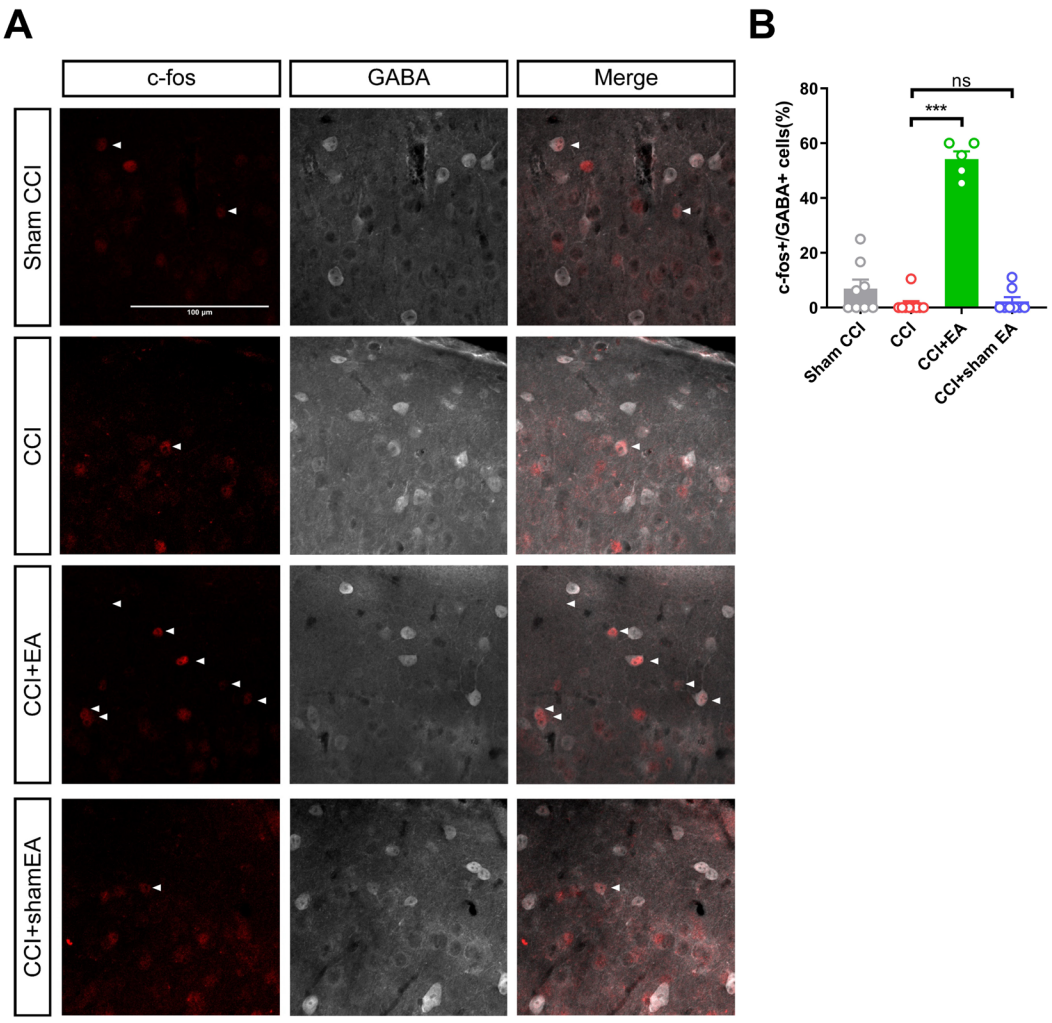

Fig. S4. EA treatment remarkably activates GABAergic neurons, Related to Figure 4. (**A**) c-Fos staining of cortical neurons in L2/3 of S1 (left), plus merging with GABA (middle and right). Scale bar, 100 μm. (**B**) EA treatment leads to a prominent c-Fos activation of GABAergic neurons (GABA+) in S1 (Kruskal-Wallis statistic=17.21, $P<0.001$; ***$P<0.001$ using Tukey post-hoc comparison; ns, no significant difference; n=8, 9, 5 and 8 animals for sham CCI, CCI, CCI+EA and CCI+sham EA group, respectively). Data are presented as mean±SEM.

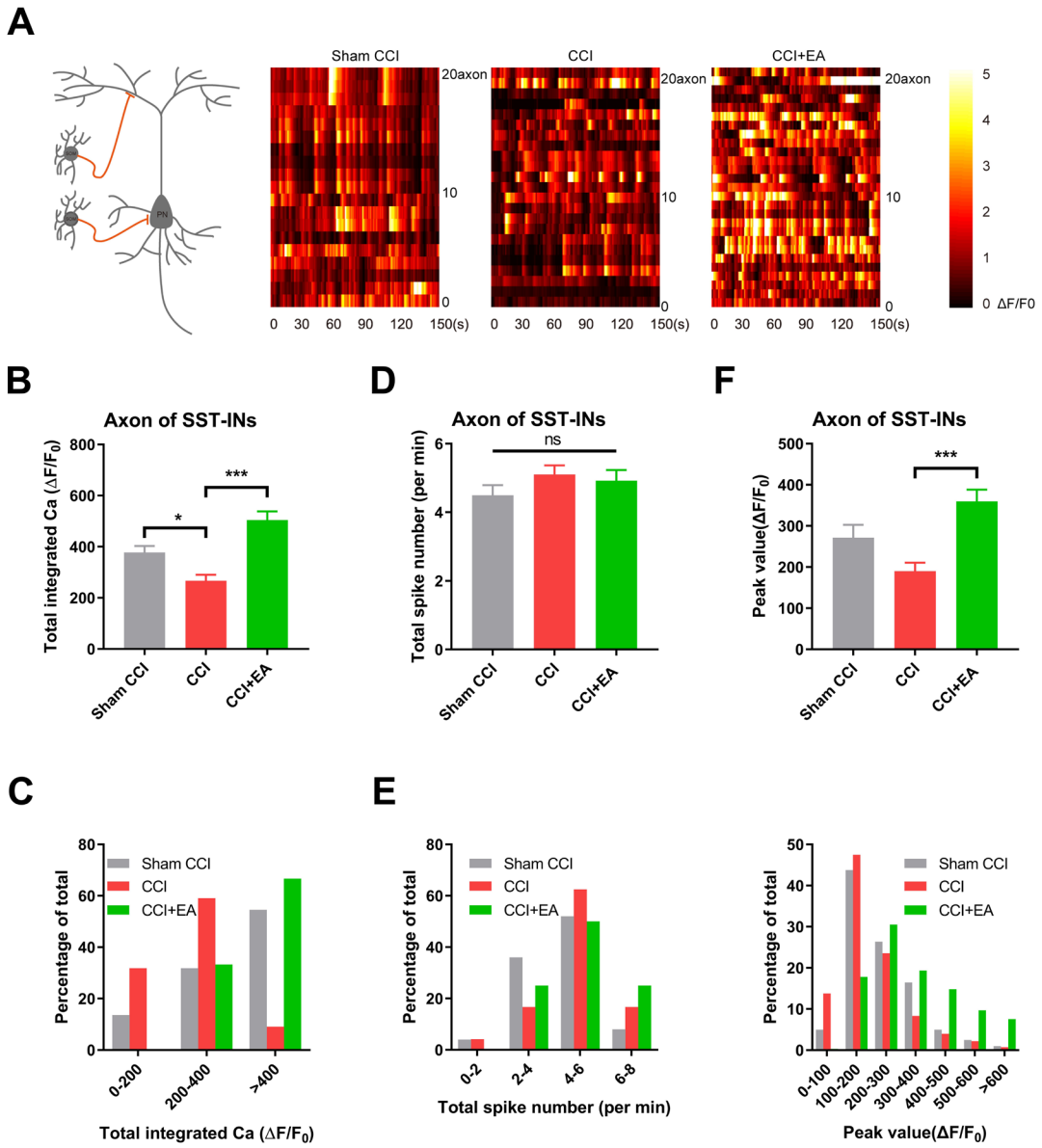

Fig. S5. EA treatment potentiates Ca^{2+} activities of SST-INs axons, Related to Figure 4. (**A**) the heat-map recording showing normalized Ca^{2+} activities ($\Delta F/F_0$) of SST-IN axons during the 150s recording period. A total of 20 representative axons were plotted from each group. (**B** to **C**) Total integrated Ca^{2+} activities in SST-IN axons were suppressed by CCI, and were re-elevated by EA. Top (**B**), averaged total integrated Ca^{2+} activities (Sham CCI: 377.5±25.41, CCI: 266.7±23.68, CCI+EA: 504.4±34.17; Kruskal-Wallis test statistic=23.17, P<0.001; *P=0.0225 between sham CCI and CCI group; ***P<0.001 between CCI and CCI+EA group using Dunn's post-hoc

comparison; *n*=23, 30 and 33 axons, *N*=3, 4 and 4 animals for sham CCI, CCI and CCI+EA group, respectively). Bottom (**C**), histogram for the frequency distribution of total integrated Ca^{2+} activities. (**D** to **E**) Ca^{2+} spike frequency (spike number per min) of SST-INs axons was not altered by CCI or EA treatment. Top (**D**), averaged Ca^{2+} spike frequency (Sham CCI: 4.47±0.30, CCI: 5.10±1.30, CCI+EA: 4.92±0.31; ns, no significant difference from Kruskal-Wallis test; *n*=25, 24 and 20 axons, *N*=3, 4 and 4 animals for sham CCI, CCI and CCI+EA group, respectively). Bottom (**E**), histogram showing the frequency distribution of Ca^{2+} spike frequency. (**F** to **G**) Peak values of Ca^{2+} activities in SST-INs axons were elevated by EA. Top (**F**), averaged peak values of Ca^{2+} activities (Sham CCI: 271.5±31.03, CCI: 190.3±20.44, CCI+EA: 359.8±28.40; Kruskal-Wallis test statistic=20.58, $P<0.001$; ***$P<0.001$ using Dunn's post-hoc comparison; *n*=25, 24 and 20 axons, *N*=3, 4 and 4 animals for sham CCI, CCI and CCI+EA group, respectively). Bottom (**G**), frequency distribution of peak values of Ca^{2+} activities. Data are presented as mean±SEM.

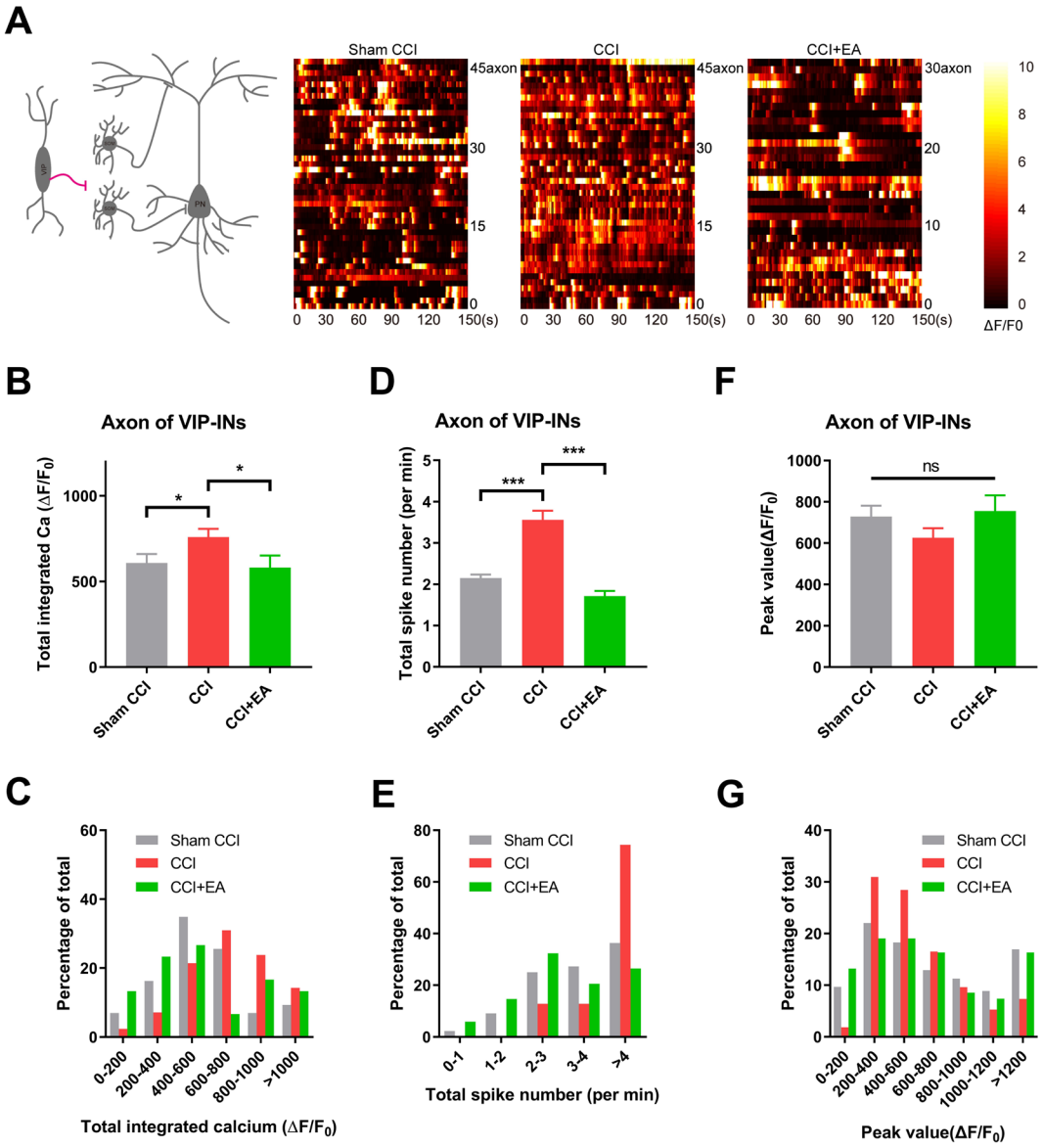

Fig. S6. EA intervention suppresses Ca^{2+} activities of VIP-INs axons, Related to Figure 5. (**A**) the representative heat-map recording showing normalized Ca^{2+} activities ($\Delta F/F_0$) of VIP-IN axons during the 150s recording period. A total of 30~45 representative axons were plotted from each group. (**B** to **C**) Total integrated Ca^{2+} activities in VIP-IN axons were elevated by CCI, and were suppressed by EA. Top (**B**), total integrated Ca^{2+} activities (Sham CCI: 608.2±52.00, CCI: 759.1±47.97, CCI+EA: 581.9±69.66; Kruskal-Wallis test statistic=9.707, P=0.0078; *P=0.0285 between sham CCI and CCI group, and P=0.0243 between CCI and CCI+EA group using Dunn's

post-hoc comparison; *n*=50, 47 and 36 axons, *N*=4, 5 and 4 animals for sham CCI, CCI and CCI+EA group, respectively). Bottom (**C**), histogram for the frequency distribution of total integrated Ca^{2+} activities. (**D** to **E**) Ca^{2+} spike frequency of VIP-INs axons was increased by CCI and was decreased after EA treatment. Top (**D**), averaged Ca^{2+} spike frequency (Sham CCI: 2.15±0.74, CCI: 3.56±0.22, CCI+EA: 1.71±0.13; Kruskal-Wallis test statistic=56.89, *P*<0.001; ***P<0.001 using Dunn's post-hoc comparison; *n*=79, 52 and 63 axons, *N*=4, 5 and 4 animals for sham CCI, CCI and CCI+EA group, respectively). Bottom (**E**), histogram showing the frequency distribution of Ca^{2+} spike frequency. (**F** to **G**) Peak values of Ca^{2+} activities in VIP-INs axons were unchanged across all groups. Top (**F**), averaged peak values of Ca^{2+} activities (Sham CCI: 729.1±51.9, CCI: 626.6±45.44, CCI+EA: 755.4±75.99; ns, no significant difference from Kruskal-Wallis test; *n*=79, 52 and 63 axons, *N*=4, 5 and 4 animals for sham CCI, CCI and CCI+EA group, respectively). Bottom (**G**), frequency distribution of peak values of Ca^{2+} activities. Data are presented as mean±SEM.

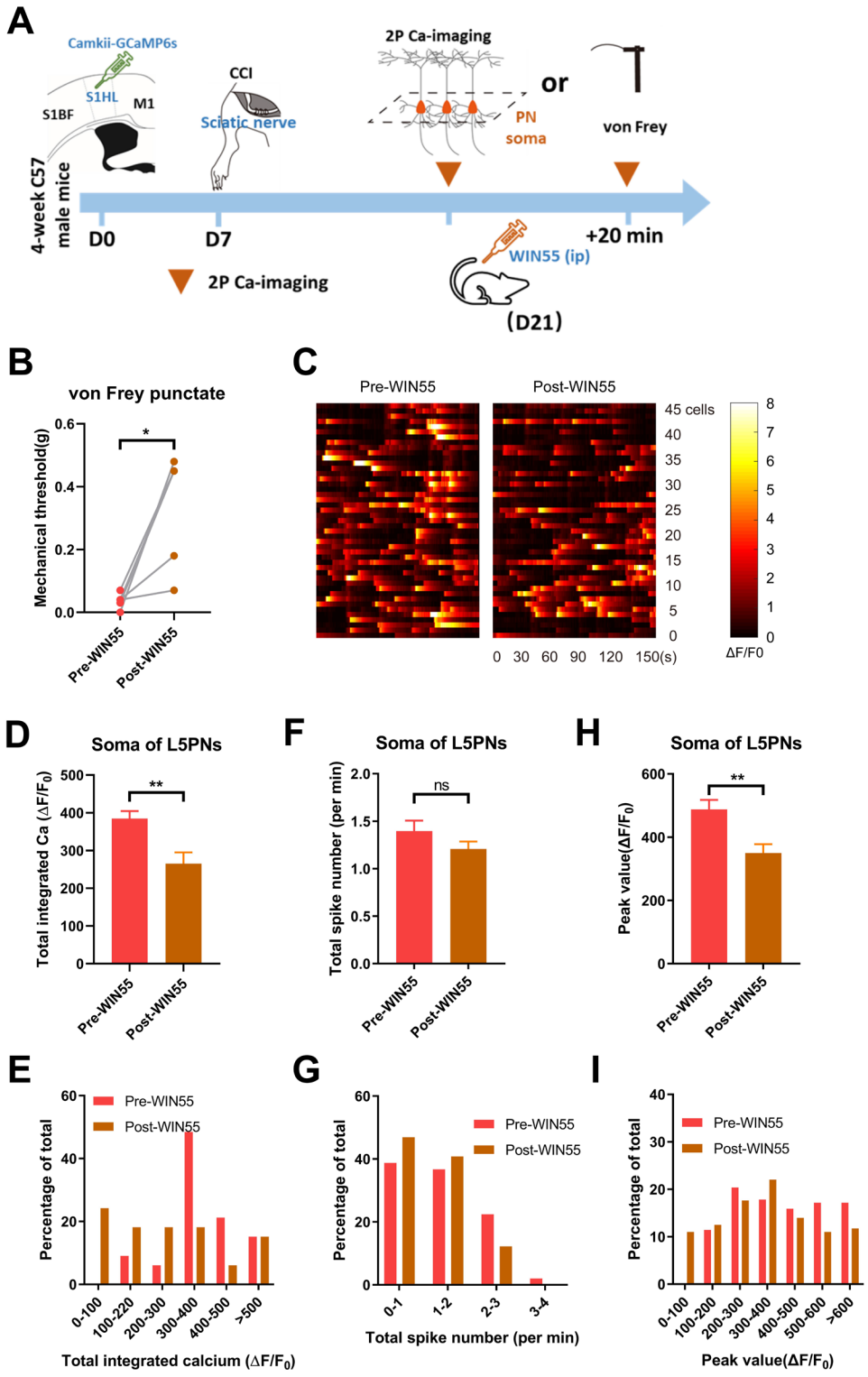

Fig. S7. Pharmaceutical activation of CB1R rapidly alleviated mechanical hypersensitivity and suppressed Ca^{2+} activities of S1, Related to Figure 6. (**A**) Schematic diagrams for experiments in **B** to **I**. Male C57 mice were transfected with GCaMP6s, and received CCI surgery

on D7. After 7 days, single intraperitoneal (ip) injection of WIN55 was applied, the mechanical threshold using von Frey and Ca^{2+} activities of L5PNs in S1 were monitored before and at 20 min after the injection. (**B**) Mechanical threshold (g) of the same animal before and after WIN55 infusion. The activation of CB1R remarkably increased the mechanical threshold (Wilcoxon matched-pairs test, P=0.0156, n=7 animals). (**C**) Heat-maps for normalized Ca^{2+} activities in L5PNs from the same group of fields of views (FOVs) before and after drug infusion. A total of 45 representative cells from 4 animals were displayed. (**D** to **E**) Total integrated Ca^{2+} activities of L5PNs soma were suppressed by WIN55. Top (**D**), total integrated Ca^{2+} activities before and after drug treatment (Pre-WIN55: 384.5±19.86, Post-WIN55: 265.2±29.88; Wilcoxon matched-pairs test, P=0.0010, n=56 neurons from 4 animals). Bottom (**E**), histogram showing the frequency distribution of total integrated Ca^{2+}. (**F** to **G**) The frequency of Ca^{2+} spikes remained unchanged. Top (**F**), the frequency of Ca^{2+} spikes before and after drug treatment (Pre-WIN55: 1.40±0.11, Post-WIN55: 1.21±0.08; Wilcoxon matched-pairs test, P=0.1026, n=56 neurons from 4 animals). Bottom (**G**), histogram showing the frequency distribution of Ca^{2+} spike frequency. (**H** to **I**) The peak value of Ca^{2+} spikes was suppressed by WIN55. Top (**H**), the peak value of Ca^{2+} spikes before and after drug treatment (Pre-WIN55: 488.0±30.04, Post-WIN55: 350.1±27.69; Wilcoxon matched-pairs test, P=0.0028, n=56 neurons from 4 animals). Bottom (**I**), the frequency distribution of Ca^{2+} peak values. Data are presented as mean±SEM.

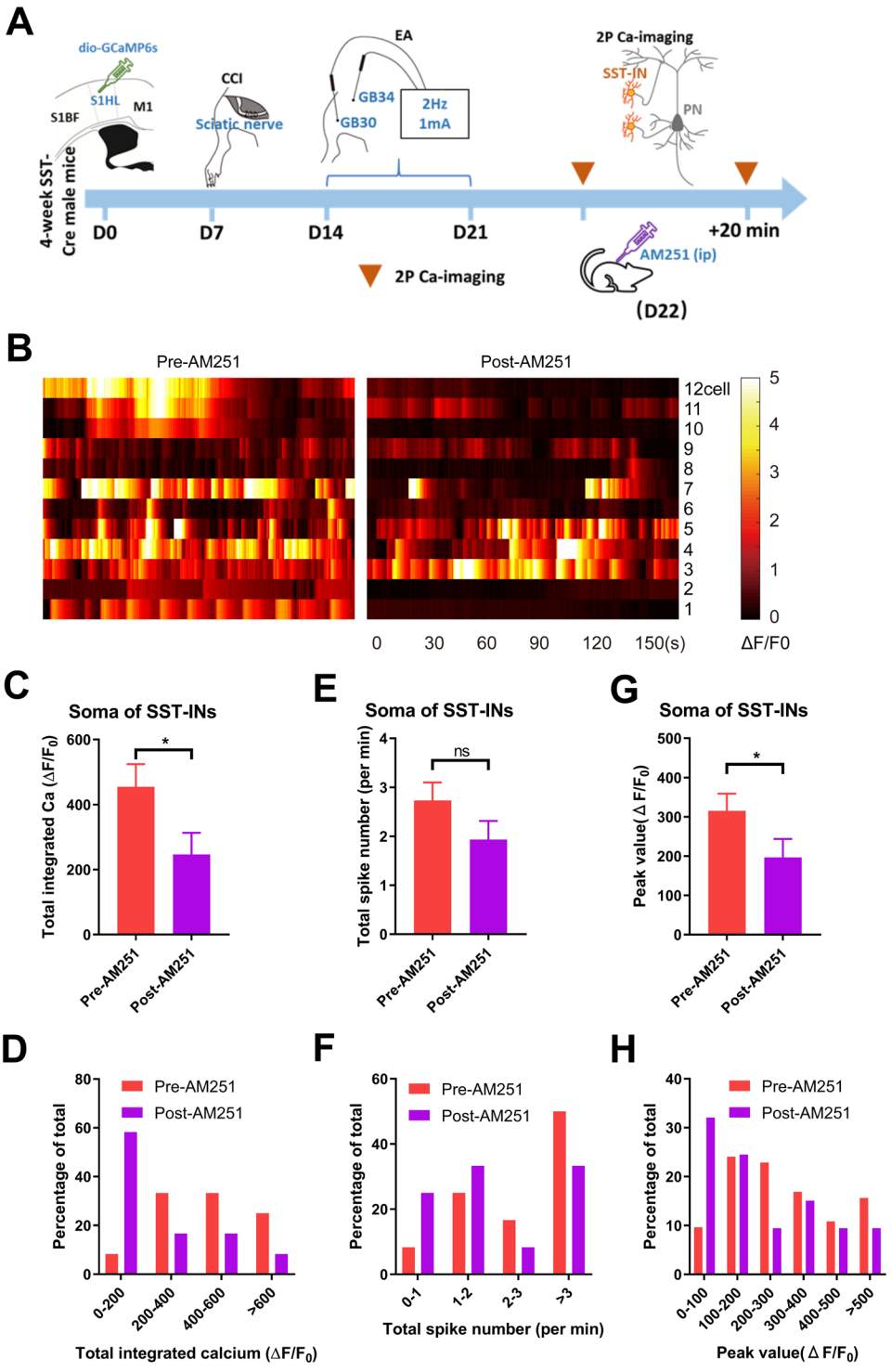

Fig. S8. Blockade of CB1R reversed the potentiation of SSI-INs by EA, Related to Figure 7.

(**A**) Schematic diagrams for experiments in **B** to **H** as similar as those in **Fig. S7A**, except the infusion of AM251 after 7-day EA intervention on SST-Cre mice. (**B**) Heat-maps for normalized Ca^{2+} activities in SST-IN soma from the same group of fields of views (FOVs) before and after drug

infusion. A total of 12 cells from 3 animals were displayed. (**C** to **D**) Total integrated Ca^{2+} activities of SST-INs soma were suppressed by AM251. Top (**C**), total integrated Ca^{2+} activities before and after drug treatment (Pre-AM251: 455.1±69.23, Post-AM251: 246.7±66.14; Wilcoxon matched-pairs test, P=0.0269, n=12 neurons from 3 animals). Bottom (**D**), histogram showing the frequency distribution of total integrated Ca^{2+}. (**E** to **F**) The frequency of Ca^{2+} spikes remained unchanged. Top (**E**), the frequency of Ca^{2+} spikes before and after drug treatment (Pre- AM251: 2.73±0.36, Post- AM251: 1.93±0.38; Wilcoxon matched-pairs test, P=0.1895, n=12 neurons from 3 animals). Bottom (**F**), histogram showing the frequency distribution of Ca^{2+} spike frequency. (**G** to **H**) The peak value of Ca^{2+} spikes was suppressed by AM251. Top (**G**), the peak value of Ca^{2+} spikes before and after drug treatment (Pre-AM251: 315.5±43.58, Post- AM251: 196.8±47.17; Paired t-test, $t(11)$=2.464, P=0.0314, n=12 neurons from 3 animals). Bottom (**H**), the frequency distribution of Ca^{2+} peak values. Data are presented as mean±SEM.

Table S1. c-Fos cell quantification and co-labelling in S1, Related to Figure 2 and Figure 4.

	Excitatory neurons (NG+) in layer 5					Inhibitory neurons (GABA+) in layer 2/3				
	Animal #	Fos+	NG+	Fos+NG+	Fos+NG+/NG+ (in %)	Animal #	Fos+	GABA+	Fos+GABA+	Fos+GABA+/GABA+ (in %)
Sham CCI	1	4	146	4	2.74	1	2	16	1	6.25
	2	6	161	6	3.73	2	1	4	1	25.00
	3	8	147	8	5.44	3	5	8	2	25.00
	4	11	156	9	5.77	4	9	12	2	16.67
	5	7	158	3	1.90	5	4	8	2	25.00
	6	3	237	3	1.27	6	2	13	1	7.69
	7	4	161	2	1.24	7	2	14	3	21.43
	8	6	127	3	2.36	8	3	13	1	7.69
CCI	1	18	156	15	9.62	1	6	14	1	7.14
	2	26	165	24	14.55	2	10	16	1	6.25
	3	18	182	15	8.24	3	8	14	0	0.00
	4	19	165	15	9.09	4	10	19	2	10.53
	5	16	174	13	7.47	5	11	8	2	25.00
	6	18	182	14	7.69	6	9	7	0	0.00
	7	20	186	17	9.14	7	7	9	2	22.22
						8	10	11	1	9.09
						9	9	12	2	16.67

CCl+ EA	1	2	143	2	1.40	1	10	10	6	60.00
	2	0	140	0	0.00	2	4	6	3	50.00
	3	1	152	1	0.66	3	7	11	5	45.45
	4	2	166	2	1.20	4	10	9	5	55.56
	5	0	156	0	0.00	5	4	7	3	42.86
	6	0	177	0	0.00					
	7	1	156	1	0.64					
	8	0	150	0	0.00					
	9	1	167	1	0.60					
CCl+ sham EA	1	25	164	20	12.20	1	8	12	1	8.33
	2	20	165	18	10.91	2	8	8	2	25.00
	3	6	151	4	2.65	3	9	8	1	12.50
	4	16	173	13	7.51	4	7	14	1	7.14
	5	19	167	18	10.78	5	9	10	3	30.00
	6	13	153	10	6.54	6	7	5	10	200.00
	7	17	181	13	7.18	7	6	9	1	11.11
	8	31	173	28	16.18	8	8	7	1	14.29
	9	40	183	35	19.13					

Table S2. Primary and secondary antibody used in Western blot and immunofluorescent blotting, related to Figure 6.

	Name	Host	Brand	Catalog#	Dilution
Western blot					
Primary antibody	anti-CB1R	Rabbit	CST	93815S	1:1 000
	anti-GAPDH	Rabbit	Abcam	ab18162	1:2 000
Secondary antibody	anti-rabbit IgG H&L (HRP)	Goat	Abcam	ab6721	1:8 000
Immunofluorescent staining					
Primary antibody	anti-c-Fos	Guinea pig	SYSY	226004	1:500
	anti-Neurogranin	Rabbit	Millipore	AB5620	1:1 000
	anti-GABA	Rabbit	Sigma	a2052	1:500
	anti-CB1R	Rabbit	CST	938155	1:500
Secondary antibody	anti-guinea pig IgG (Alexa Fluor® 488)	Goat	Invitrogen	A-11073	1:500
	anti-rabbit IgG (Alexa Fluor® 594)	Goat	Abcam	ab150077	1:500